Journal Pre-proofs

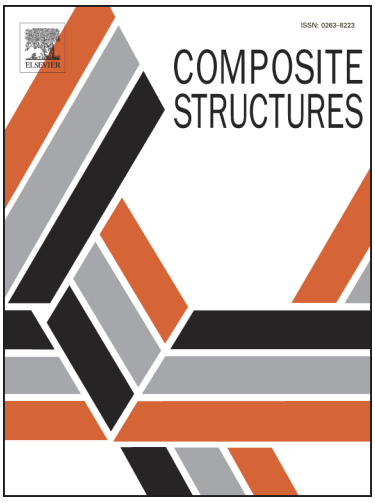

Discrete modelling of externally bonded composite layers on masonry structures

F. Cannizzaro, B. Pantò, S. Caddemi, I. Caliò

PII: S0263-8223(23)00281-7
DOI: https://doi.org/10.1016/j.compstruct.2023.116937
Reference: COST 116937

To appear in: *Composite Structures*

Received Date: 28 June 2021
Revised Date: 8 February 2023
Accepted Date: 16 March 2023

Please cite this article as: Cannizzaro, F., Pantò, B., Caddemi, S., Caliò, I., Discrete modelling of externally bonded composite layers on masonry structures, *Composite Structures* (2023), doi: https://doi.org/10.1016/j.compstruct.2023.116937

Discrete modelling of externally bonded composite layers on masonry structures

F. Cannizzaro[a], B. Pantò[b], S. Caddemi[a], I. Caliò[a]

[a]: *Department of Civil Engineering and Architecture, Università di Catania, Via Santa Sofia 64, Catania, Italy*
[b]: *Department of Civil and Environmental Engineering, Durham University, Durham, UK*

Abstract

The safeguard of existing masonry structures requires the adoption of structural retrofitting strategies able to preserve the architectural of the construction. Numerous strengthening techniques are available for the rehabilitation of exitsting structures, including historic and monumental buildings, most of them based on the application of Externally Bonded Composite (EBC) layers on the masonry surfaces. Such a technique represents a low-invasive retrofitting strategy widely used in engineering practice. In this paper, within the framework of the Discrete Macro-Element Method (DMEM) already introduced by the authors, an original macro-element for modelling the interaction between masonry elements and EBC layers is presented. The proposed model is able to provide a reliable simulation of the EBC layer applications to masonry structures although maintaining a low computational burden. After a theoretical description of the EBC macro-element, the new macro-modelling approach is validated against experimental and numerical tests available in the literature.

Keywords: *Masonry Structures; Macro-models; Externally Bonded Composites; Discrete Element Method; Discrete Macro-Element Method; Computational modelling.*

Corresponding author: Francesco Cannizzaro, e-mail: *francesco.cannizzaro@unict.it*, tel: +390957382275

1. Introduction

The maintenance and restoration of existing structures, including historic and monumental masonry buildings, require ad hoc strategies able to guarantee the preservation of the original structural scheme and the architectural and historic value. Therefore, retrofitting techniques should be characterized by low invasiveness and reversibility. Reinforcement of masonry structures by means of the application of FRP (Fibre Reinforced Polymer) or, more recently, by means of FRCM (Fiber Reinforced Cementitious Matrix) composites nowadays represent commonly adopted retrofitting techniques due to their simplicity of application, low weight, adaptivity to curved geometry, low invasiveness [1] time and cost of installation [2],[3], and vapour permeability in the case of FRCM systems. The fibre reinforcement materials can be constituted by organic (e.g., carbon) or inorganic (e.g., glass or basalt) fibres. The adherence with the masonry surface can be realized by means of epoxy resins in the case of FRP systems or, alternatively, organic matrix, such as lime or cementitious mortar in the case of FRCM systems. The fibre-reinforced composite material can be applied to the masonry support through one-dimensional (i.e. strips) or bi-dimensional (i.e. layers) layouts.

Both of the above-mentioned reinforcement techniques are applied on the external surface of the masonry and for that reason can be addressed to as Externally Bonded Composites (EBC). EBC-reinforced masonry structures exhibit a highly non-linear behaviour due to the complex interaction between the EBC material and the masonry support. Several experimental tests have been performed on EBC-reinforced masonry structural elements aimed at investigating various aspects such as: *i*) the interaction between EBC and masonry

[4]-[8], *ii*) the in-plane shear response of a reinforced masonry panel [9],[10], *iii*) the out of plane response of reinforced masonry walls [11],[12], *iv*) the ultimate behaviour of EBC curved masonry structures such as arches and vaults under different loading contitions [13],[14], *v*) the efficacy of different reinforcement typologies and their geometrical arrangements [15]-[17].

The collapse mechanisms related to the EBC materials are related to the sheer rupture in tension of the reinforcement itself, or its debonding from the masonry support. In this regard, two main bond-failure mechanisms between the reinforcement and the masonry support can occur, usually classified as normal pure opening (mode I) and shear bond-slip (mode II) [18], associated with normal tensile and shear stresses at the EBC-masonry interface, respectively. In the case of FRCM systems the debonding mechanisms can occur following different modes, as effectively described in [19],[20]. In particular, damage can occur in the substrate, at the reinforcement-to-substrate interface with a complete detachment of the reinforcement, and at the textile-to-matrix interface, with sliding of the textile within the reinforcement thickness, and with tensile rupture of the textile.

Given the experimental evidence of the EBC reinforcement efficacy, attention has been devoted in the literature to a proper modelling of the interaction between EBC and masonry support considered on masonry modelling strategies. To describe the complex non-linear EBC-masonry interaction many contributions have been provided to formulate suitable constitutive laws for the shear-stress transfer mechanisms between the EBC layers and the

flat or curved masonry supports. The simplest of these analytical formulations is a bilinear law proposed in the Italian guidelines [21]. Other more complex strategies, able to consider combined damage mechanisms, can be found in [22]-[27]. Concerning the FRCM technique, an analytical rigid-trilinear cohesive law for simulating the bond-slip behaviour, was recently proposed in [26]. A theoretical formulation accounting for the bond-slip behaviour on curved surfaces has been proposed in [28]. Alternatively, a simplified model based on a spring-model strategy has been presented in [29] and validated in [30].

Generally speaking, detailed modelling of masonry structures reinforced with EBC for the simulation of their complex non-linear behaviour can be performed by refined Finite Element descriptions. Detailed simulations employing three-dimensional elements considering finite element meso-scale approaches have been performed in [31]-[35] or limit analysis [36]-[38] have been performed to assess the ultimate behaviour of EBC-reinforced masonry structures.

However, it is widely recognised that these approaches are computationally demanding and unsuitable for large systems. For the latter reason, different strategies that drastically reduce the computational cost and providing sufficiently accurate results, have been proposed in the literature [39]-[42]. A low-cost and reliable finite element model, specifically conceived for the analysis of EBC-reinforced masonry arches, has been recently proposed by Bertolesi et al. [39]. In this approach the reinforcing fibres are modelled by means of 2-node truss elements characterised by elastic-brittle behaviour in tension and no strength in compression. A more detailed modelling strategy that can be used at the macro-scale can be

found in [40], where six-nodes wedges describe masonry and the EBC material is described by three-node flat elements. Finally, the interaction between masonry and EBC elements is simulated by means of triplets of springs which govern the debonding phenomenon between the EBC material and the masonry support. Such an approach is combined with a Sequential Quadratic Programming (SQP) solving strategy, able to identify subsequent stages of the non-linear status of the structure, considering approximated constitutive laws by means of a piecewise constant discontinuous function [41]. A further macro-modelling approach relying on a two-step discrete homogenization technique capable of capturing the average properties of FRCM reinforced masonry portions has been recently proposed [42]. Precisely, masonry is described by elastic cells linked by homogenized interfaces, where the non-linearities are lumped. In contrast, the 2D fibre-reinforced grid is described by elastic-plastic trusses and additional layers of solid elements represent the cementitious matrix.

Within the context of the macro-modelling approaches, this paper addresses the modelling of EBC reinforcing techniques in the Discrete Macro Element Model (DMEM) framework, able to simulate the non-linear response of unreinforced masonry structures, introduced by the authors in the last decade [43]-[46]. In particular, this study completes and extends a novel simplified approach recently sketched by the authors [47][48], and also responds to a validation request, concerning available experimental data. Zero thickness flat rigids element accounting for the presence of EBC strips or layers along the masonry surface, are devised. These macro-elements are connected to each other by means of non-linear one-dimensional

continuous interfaces; in addition, a novel continuous bi-dimensional non-linear interface, entitled to model the interaction between the EBC layer and the masonry, is introduced. The continuous one-dimensional EBC-EBC interfaces are conceived to model the non-linear tensile behaviour of the composite as well as the tensile rupture of the textile. On the other hand, the continuous plane EBC-masonry interface is formulated to simulate the debonding phenomenon due to mode I and mode II mechanisms.

The proposed strategy possesses some advantages with respect to other simplified models. The DMEM allows to strongly reduce the computational burden being characterised by very few degrees of freedom and allowing non-conforming mesh discretizations. The proposed strategy is able to grasp the progressive transfer of the shear stresses between the EBC strips and the masonry support and to explicitly distinguish the failure modes of the EBC-EBC (tensile failure) and the EBC-masonry interfaces by shear failure. It is particularly suitable simulating curved geometry masonry structures, such as arches, vaults, domes etc including the elements with continuous section variability still mantaining a very low computational cost. In view of the above consideration the model can be considered sufficiently accurate although simplified, and particularly suitable for practical engineering purposes.

In this paper the model is validated against experimental bond-slip tests performed on straight and curved specimens [50], out-of-plane loaded EBC-reinforced masonry panels [49] and arches [50][51]. The results are also compared with other numerical simulations [39],[50] showing the effectiveness and the accuracy of the proposed simplified numerical strategy.

2. The modelling strategy: discrete macro-element for the EBC coating

The proposed approach aims at modelling the presence of EBC coating attached to the masonry support under the form of strips or layers. The approach relies on the formulation of a novel macro-element applied in accordance with the real position of the EBC strips or layers to simulate the non-linear behaviour and the corresponding failure mechanism of the reinforcement and its interaction with the masonry substrate. The masonry structure is described according to a three-dimensional discrete macro-model formulated to simulate the behaviour of unreinforced masonry structures [46][52]-[55] also in presense of curved geometry [44],[45],[56].

The EBC textile reinforcement is modelled through quadrilateral flat macro-elements connected to the contiguous macro-elements by means of one-dimensional zero-thickness continuous interfaces entitled to govern the non-linear behaviour in traction of the composite material. Precisely, the element deformability is lumped at each one-dimensional interface embedding the contribution of the fibres along the direction orthogonal to the interface length. The disposal of interfaces along two opposite sides of the new EBC macro-element applies to strip modelling; on the other hand, interfaces applied to four sides of the EBC macro-element is an efficacious strategy to model 2D grid-type fibre reinforcements, even with anisotropic characteristics, able to represent the application of EBC layers. The mechanical scheme for the proposed modelling of a EBC textile is depicted in **Error! Reference source not found.** coupled with a DMEM of the masonry support where the contiguous zero thickness EBC-EBC interfaces are represented as thin rectangles.

The interaction between the EBC coating and the masonry element is modelled by a plane continuous non-linear interface, with zero-thickness and a three-dimensional behaviour, that is entitled to simulate the presence of the adhesive, organic or cementitious matrix, as also depicted in **Error! Reference source not found.**. The plane interface between EBC elements and the masonry support is conceived to model the transfer of the normal and tangential stress between the reinforcement and the masonry. By doing so, the bond-shear and bond-tensile behaviour of the mortar layer connecting the EBC textile to the masonry can be adequately described.

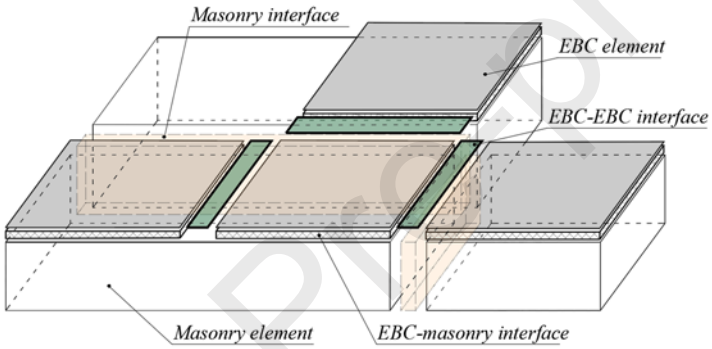

Figure 1. Figure 1 EBC coating macro-model attached to the front (rear) of the masonry macro elements according to strip or layer patterns

It is worth noticing that the proposed mechanical scheme is not limited to the case of EBC macro-elements applied on the front/rear surfaces of masonry elements and with sides parallel to the masonry element edges, as in **Error! Reference source not found.**. In fact, other layouts with different orientation of the EBC elements (Figure 2a) as well as along the perimeter of the masonry macro-elements can be simulated (**Error! Reference source not found.**).

Although the proposed approach is not devoted to a micro-modelling of EBC-reinforced masonry elements, it can be applied to model reinforcement layouts useful for applications in engineering practice. In fact, the above-described reinforcement schemes can be repeated to model applications of composite coating on masonry portions with curved geometry (vaults or domes) using of irregular macro-elements both for the EBC reinforcement and the masonry support. One example is reported in **Error! Reference source not found.**.

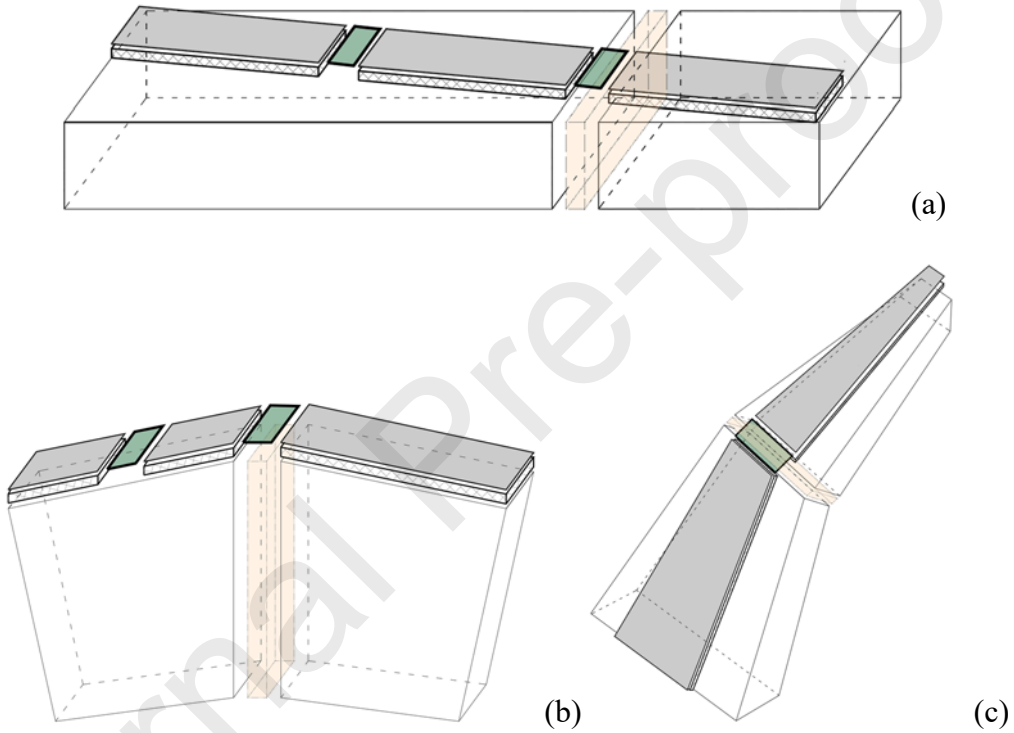

Figure 2. Strip coating macro-model attached to: a) the front (rear) of the masonry macro elements with strips not parallel to the masonry element edges; b) to the perimeter of the masonry macro elements; c) to the front (rear) or perimeter of irregular masonry macro elements adopted for curved geometry.

In addition, crossed/overlapped reinforcing elements can be considered provided that only the needed interfaces are created (i.e. crossed reinforcing strips do not interact with each other).

3. Kinematics of the interfaces

The macro-element to model the EBC layers can be regarded as a rigid plate where the relevant deformability and non-linear behaviour are ruled by the EBC-EBC and EBC-masonry interfaces. The kinematics of the interfaces related to the Lagrangian parameters of the connected macro-elements is described in the following sub-sections. The definition of their mechanical behaviour will then be addressed in the next section.

3.1. The EBC-EBC interface

With regard to a local reference system ($\mathbf{e}_x, \mathbf{e}_y, \mathbf{e}_z$), as in Figure 3a and better detailed in Appendix A, the generic *r*-th EBC macro-element is characterized by six (translations and rotations of the centre of gravity G) rigid-body degrees of freedom collected in the vector $\mathbf{d}_r^T = \left[U_r \quad V_r \quad W_r \quad \Phi_r \quad \Theta_r \quad \Psi_r\right]$ (Figure 3b).

The zero-thickness one-dimensional interface, connecting two *r* and *s* adjacent EBC rigid elements, lies between contact edges of contiguous elements and is conceived to rule the non-linear behaviour along a specified direction of the EBC reinforcement. A local reference system ($\mathbf{e}_\xi, \mathbf{e}_\eta, \mathbf{e}_\zeta$) with the origin located at the midpoint Ω of the EBC-EBC interface is assumed as in Figure 3a and better specified in Appendix A. At the generic coordinate ξ,

ranging in the interval $\left[-l_i/2\,,l_i/2\right]$ where l_i is the length of the interface, the displacements of the interface edges corresponding to the *r* and *s* elements expressed in the interface local reference system are denoted as $\mathbf{u}_r^T(\xi)=\left[u_r(\xi)\quad v_r(\xi)\quad w_r(\xi)\right]$ and $\mathbf{u}_s^T(\xi)=\left[u_s(\xi)\quad v_s(\xi)\quad w_s(\xi)\right]$, respectively. In Figure 3c the specific case of coplanar EBC plate elements lying on the global XY plane is depicted. $\mathbf{u}_r(\xi)$ and $\mathbf{u}_s(\xi)$ can be expressed in terms of the middle point displacements and the rotations of the *r*-th and *s*-th elements (auxiliary degrees of freedom represented in Figure 3b and collected in the vectors $\overline{\mathbf{u}}_r^T=\left[u_r\quad v_r\quad w_r\quad \phi_r\quad \theta_r\quad \psi_r\right]$ and $\overline{\mathbf{u}}_s^T=\left[u_s\quad v_s\quad w_s\quad \phi_s\quad \theta_s\quad \psi_s\right]$, respectively) as follows:

$$\mathbf{u}_r(\xi)=\mathbf{N}_f(\xi)\overline{\mathbf{u}}_r \qquad\qquad \mathbf{u}_s(\xi)=\mathbf{N}_f(\xi)\overline{\mathbf{u}}_s \tag{1}$$

where

$$\mathbf{N}_f(\xi)=\begin{bmatrix}1&0&0&0&0&0\\0&1&0&0&0&\xi\\0&0&1&0&-\xi&0\end{bmatrix} \tag{2}$$

On the other hand, the relationships between the auxiliary degrees of freedom $\overline{\mathbf{u}}_r^T$ and $\overline{\mathbf{u}}_s^T$, and the Lagrangian parameters of the *r*-th and *s*-th elements collected in the vectors $\mathbf{d}_r\,,\mathbf{d}_s$, governing the EBC element kinematics, can be expressed as follows

$$\overline{\mathbf{u}}_r=\mathbf{A}_r\,\mathbf{d}_r \quad ; \qquad \overline{\mathbf{u}}_s=\mathbf{A}_s\,\mathbf{d}_s \tag{3}$$

where the $\mathbf{A}_r, \mathbf{A}_s$ 6×6 compatibility matrix operators have been introduced and fully defined in Appendix A.

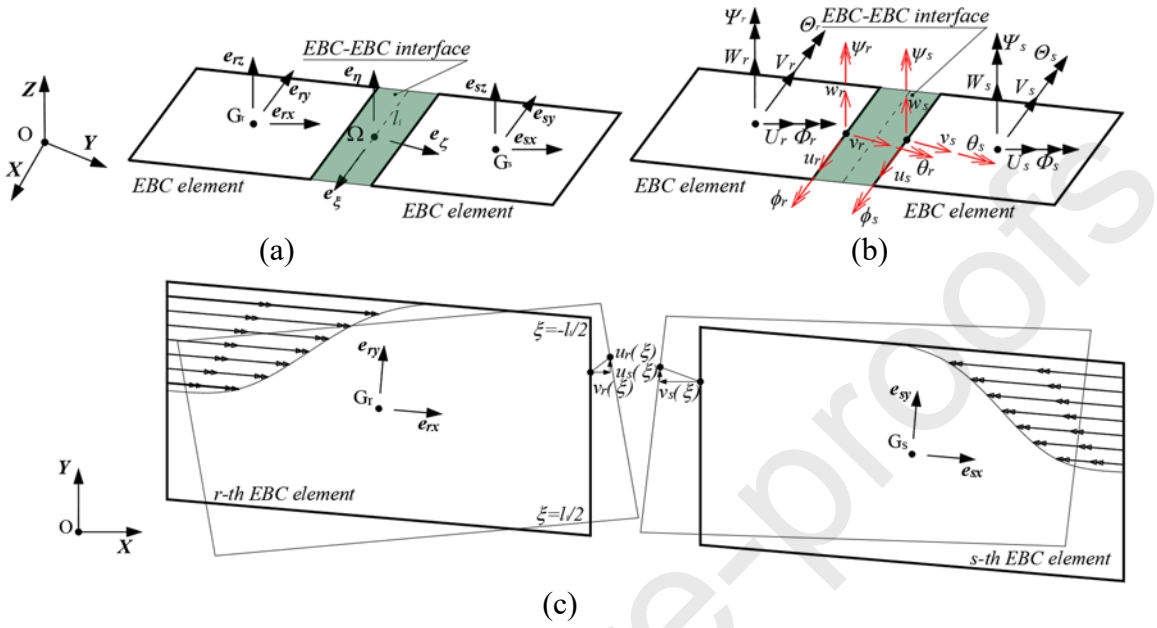

Figure 3. EBC elements and the relevant EBC-EBC interface: (a) reference systems, (b) degrees of freedom and (c) relative displacements at the interface in the case of coplanar EBC plate elements

In view of Eqs. (1)-(3), the local displacements $\mathbf{u}_r(\xi)$ and $\mathbf{u}_s(\xi)$ along the two edges of the interface can be expressed as a function of the Lagrangian parameters collected in the vectors $\mathbf{d}_r, \mathbf{d}_s$ of the *r*-th and *s*-th EBC elements, respectively, as follows:

$$\mathbf{u}_r(\xi) = \mathbf{N}_f(\xi)\mathbf{A}_r\mathbf{d}_r \quad ; \qquad \mathbf{u}_s(\xi) = \mathbf{N}_f(\xi)\mathbf{A}_s\mathbf{d}_r \tag{4}$$

Finally, based on Eq. (4), the relative displacement function $\hat{m}(\xi)$ of the interface connecting the *r*-th and *s*-th EBC elements can be expressed as follows:

$$\hat{m}(\xi) = \left[\mathbf{N}_f(\xi)\mathbf{A}_r\mathbf{d}_r - \mathbf{N}_f(\xi)\mathbf{A}_s\mathbf{d}_s\right]^T \mathbf{e}_\zeta \tag{5}$$

3.2. The EBC-masonry interface

The kinematics of the EBC-masonry interface connecting the EBC elements with the masonry macro-elements is presented in this section. The relationships between the local kinematic parameters of the interface and the Lagrangian parameters of the two connected elements (EBC plate and masonry panel) are formulated.

The generic *p*-th 3D masonry macro-element (defined, in accordance to the DMEM approach, as a shear deformable regular or irregular quadrilateral with rigid sides) is endowed with 7 degrees of freedoms $\mathbf{d}_p^T = \begin{bmatrix} U_p & V_p & W_p & \Phi_p & \Theta_p & \Psi_p & \Gamma_p \end{bmatrix}$, referred to a local reference system $\mathbf{e}_{px}, \mathbf{e}_{py}, \mathbf{e}_{pz}$. The three translations U_p, V_p, W_p and the three rotations Φ_p, Θ_p, Ψ_p of the centre of gravity G of the masonry macro-element are associated with the spatial rigid body motion of the element, while Γ_p is associated with the generalised shear deformation, as expressed in detail in [44] (Figure 4).

The interaction between the flat EBC element and the attached masonry macro-element is described by a bi-dimensional quadrilateral interface covering an area, denoted as A_{int}, lying on the front/rear surface (or along the perimeter) of the masonry element (Figure 4a). Each EBC-masonry interface is modelled by two rigid plates whose kinematics is governed by 6 degrees of freedom each (denoted as auxiliary degrees of freedom), which are duly inherited by the connected *r*-th EBC and *p*-th masonry elements, as better described in what follows.

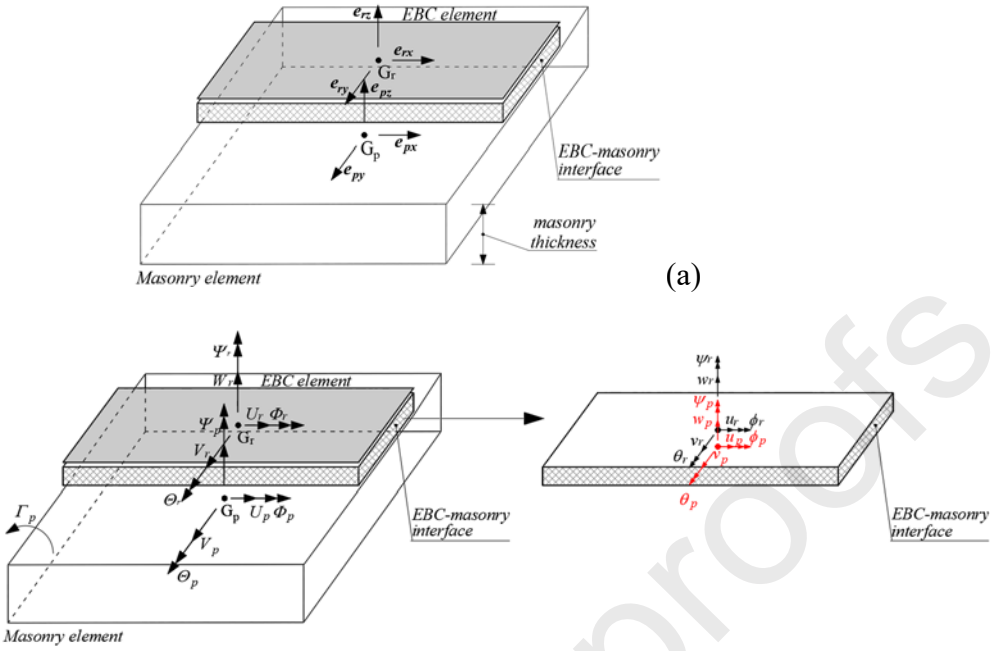

Figure 4. EBC-masonry interface: (a) reference systems, (b) degrees of freedom of the EBC and masonry element and (c) auxiliary degrees of freedom of the interface

By assuming a local reference system ($\mathbf{e}_{\xi}, \mathbf{e}_{\eta}, \mathbf{e}_{\zeta}$) coincident with the reference system ($\mathbf{e}_{rx}, \mathbf{e}_{ry}, \mathbf{e}_{rz}$) of the EBC element (Figure 4a), two local coordinates ξ and η are introduced on the interface plane and its kinematics is defined by the local displacements $\mathbf{u}_r^T(\xi,\eta) = \left[u_r(\xi,\eta) \quad v_r(\xi,\eta) \quad w_r(\xi,\eta)\right]$ and $\mathbf{u}_p^T(\xi,\eta) = \left[u_p(\xi,\eta) \quad v_p(\xi,\eta) \quad w_p(\xi,\eta)\right]$ of the (ξ,η) points of the two plates confining the interface itself. The latter two vectors can be expressed in terms of 12 auxiliary local degrees of freedom (namely the three translations and the three rotations of the two plates in correspondence of the centre of gravity G_r of the EBC element) oriented along the axes of the reference system, and conveniently collected in

the two vectors $\bar{\mathbf{u}}_r^T = \begin{bmatrix} u_r & v_r & w_r & \phi_r & \theta_r & \psi_r \end{bmatrix}$ and $\bar{\mathbf{u}}_p^T = \begin{bmatrix} u_p & v_p & w_p & \phi_p & \theta_p & \psi_p \end{bmatrix}$ (Figure 4c), which govern the kinematics of the two opposite rigid plates, as follows:

$$\mathbf{u}_r(\xi,\eta) = \mathbf{N}(\xi,\eta)\bar{\mathbf{u}}_r \qquad \mathbf{u}_p(\xi,\eta) = \mathbf{N}(\xi,\eta)\bar{\mathbf{u}}_p \tag{6}$$

where the following $\mathbf{N}(\xi,\eta)$ matrix is also introduced.

$$\mathbf{N}(\xi,\eta) = \begin{bmatrix} 1 & 0 & 0 & 0 & 0 & \eta \\ 0 & 1 & 0 & 0 & 0 & -\xi \\ 0 & 0 & 1 & -\eta & \xi & 0 \end{bmatrix} \tag{7}$$

The 12 auxiliary local degrees of freedom of the two *r, p* plates of the EBC-masonry interface, collected in the vectors $\bar{\mathbf{u}}_r, \bar{\mathbf{u}}_p$, can be in turn related to the global Lagrangian parameter vectors $\mathbf{d}_r, \mathbf{d}_p$ of the connected EBC and masonry elements, respectively, as follows:

$$\bar{\mathbf{u}}_r = \mathbf{A}_r \mathbf{d}_r \qquad \bar{\mathbf{u}}_p = \mathbf{A}_p \mathbf{d}_p \tag{8}$$

where the 6×6 matrix $\mathbf{A}_r$ and the 6×7 matrix $\mathbf{A}_p$ are compatibility matrices duly defined in Appendix B.

In view of Eq. (8) the local displacements of the (ξ,η) points of the two plates, provided by Eq. (6), can be expressed in terms of the EBC and masonry element degrees of freedoms as follows:

$$\mathbf{u}_r(\xi,\eta) = \mathbf{N}(\xi,\eta)\mathbf{A}_r\mathbf{d}_r \quad ; \quad \mathbf{u}_p(\xi,\eta) = \mathbf{N}(\xi,\eta)\mathbf{A}_p\mathbf{d}_p \tag{9}$$

On account of Eq. (9), the relative displacement vector function $\hat{\mathbf{u}}_{r,p}(\xi,\eta)=\mathbf{u}_r(\xi,\eta)-\mathbf{u}_p(\xi,\eta)$ entitled to describe the deformation of the EBC-masonry interface can be expressed as follows:

$$\hat{\mathbf{u}}_{r,p}(\xi,\eta)=\begin{bmatrix}\hat{u}_{r,p}(\xi,\eta)\\ \hat{v}_{r,p}(\xi,\eta)\\ \hat{w}_{r,p}(\xi,\eta)\end{bmatrix}=\mathbf{N}(\xi,\eta)\mathbf{A}_r\mathbf{d}_r-\mathbf{N}(\xi,\eta)\mathbf{A}_p\mathbf{d}_p \tag{10}$$

4. EBC-EBC interface mechanical behaviour

As already discussed in section 2, the mechanical characteristics of the composite textile are concentrated at the EBC-EBC interfaces. In particular, the latter are responsible for the modelling of the textile non-linear axial/flexural behaviour while the EBC shear stiffness orthogonal to the fibre direction is neglected. In the following sub-sections 4.1 and 4.2 the stiffness matrix for the EBC-EBC interface and the adopted non-linear constitutive laws, respectively, are proposed and explicitly formulated.

4.1. EBC-EBC interface stiffness matrix

The zero-thickness one dimensional uniaxial EBC-EBC interfaces are characterised by a non-linear behaviour described by the incremental relationship between the increments of the internal force distribution $\mathrm{d}f(\xi)$ along the interface axis and the increment $\mathrm{d}\hat{m}(\xi)$ of the relative displacement $\hat{m}(\xi)$, introduced in Eq. (5), as follows:

$$\mathrm{d}f(\xi)=k_T(\xi)\mathrm{d}\hat{m}(\xi) \tag{11}$$

where $k_T(\xi)$ represents the tangent stiffness distribution of the EBC-EBC interface along the local coordinate ξ.

In view of Eq. (5), the force increment $\mathrm{d}f(\xi)$ of the EBC-EBC interface, given by Eq. (11), can be also expressed as function of the degrees of freedom increment vectors of the *r*-th and *s*-th connected elements, denoted as $\mathrm{d}\mathbf{d}_r, \mathrm{d}\mathbf{d}_s$, as follows:

$$\mathrm{d}f(\xi) = k_T(\xi)\left[\mathbf{N}_f(\xi)\mathbf{A}_r\mathrm{d}\mathbf{d}_r - \mathbf{N}_f(\xi)\mathbf{A}_s\mathrm{d}\mathbf{d}_s\right]^T \mathbf{e}_\zeta \tag{12}$$

Considering Eq. (12), upon application of the principle of virtual work, the 12×12 tangent stiffness matrix of the EBC-EBC interface, related to the global degrees of freedom of the two adjacent *r*,*s* elements is obtained as follows:

$$\mathbf{K}_f = \int_0^{l_i} \mathbf{A}_f^T \tilde{\mathbf{N}}_f^T(\xi) k_T(\xi) \tilde{\mathbf{N}}_f(\xi) \mathbf{A}_f d\xi \tag{13}$$

being

$$\mathbf{A}_f = \begin{bmatrix} \mathbf{A}_r & \mathbf{0} \\ \mathbf{0} & \mathbf{A}_s \end{bmatrix}; \qquad \tilde{\mathbf{N}}_f^T(\xi) = \begin{bmatrix} \mathbf{N}_f(\xi) & -\mathbf{N}_f(\xi) \end{bmatrix} \tag{14}$$

The tangent stiffness matrix $\mathbf{K}_f$ rules the non-linear behaviour of the EBC-EBC interface and its current value is related to the tangent interface stiffness distribution $k_T(\xi)$ which is given once the constitutive behaviour of the EBC textile is duly defined as reported in the following sub-section.

4.2. EBC-EBC interface non-linear constitutive law

According to the proposed model, the EBC- EBC interface stiffness matrix is representative of the elastic/inelastic axial and flexural behaviours of adjacent portions of EBC elements, considered as an equivalent homogeneous medium. Based on the latter assumption, the tangent interface stiffness distribution $k_T(\xi)$ inherits the behaviour of the EBC textile in accordance with a specified uniaxial non-linear constitutive law of the EBC textile.

The constitutive law adopted for the EBC textile is elastic-brittle in tension with tensile strength σ_y, Young's modulus E_f, and ultimate strain ε_y, while compression force cannot be exerted (Figure 5a). It is worth to mention that the adoption of an elastic-brittle constitutive behaviour is a simplified choice representative of the textile only that does not take into account the contribution of a mortar layer which might be significant in the case of FRCM technique (at least before cracking). On the other hand, the proposed formulation of EBC-EBC interface can accommodate more complex constitutive behaviours. In the case of FRCM technique a more sophisticated constitutive law, able to account for the mortar cracking [61], would be more appropriate (for example by adopting the constitutive laws proposed in [62],[63]).

The constitutive properties of the EBC textile depicted in Figure 5a are concentrated at the EBC-EBC interface by considering an effective thickness, denoted by t_f, and an influence length over the adjacent EBC element, denoted by $l_f(\xi)$ (Figure 5b). Precisely, the chosen

constitutive law at the generic abscissa ξ of the interface is reformulated in the force distribution-relative displacement $f, \hat{m}$ plane where $f = \sigma t_f$ and $\hat{m} = \varepsilon l_f$.

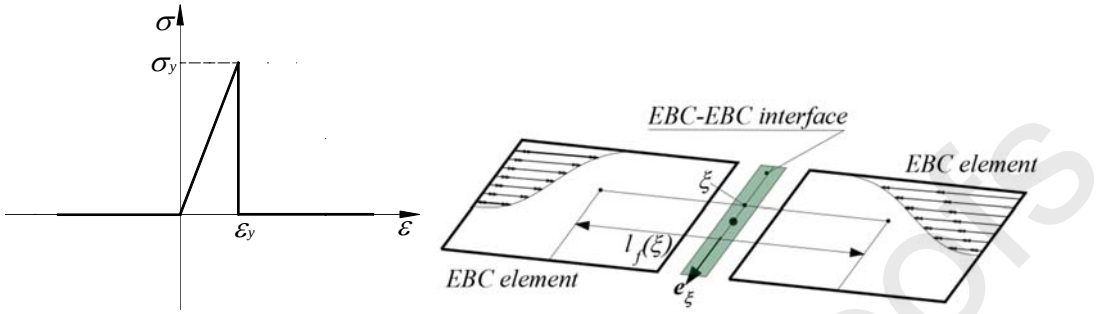

(a) (b)

Figure 5. (a) Mechanical characterization of the constitutive law relative to the EBC textile and (b) influence length of the EBC-EBC interface.

On account of the latter definitions, the tangent stiffness distribution of the EBC-EBC interface along the abscissa $0 \le \xi \le l_i$ is obtained as follows:

$$\begin{aligned} k_T(\xi) &= \frac{E_f t_f}{l_f(\xi)} \quad \text{for} \quad 0 < \hat{m} < \hat{m}_y = \varepsilon_y l_f \\ k_T(\xi) &= 0 \qquad \text{for} \quad \hat{m} \ge \hat{m}_y = \varepsilon_y l_f \quad \text{or} \qquad \hat{m} \le 0 \end{aligned} \tag{15}$$

where $\hat{m}_y$ represents the ultimate relative displacement of the interface which is reached at the relevant tensile force per unit length $f_y = \sigma_y t_f$.

Once the tangent stiffness distribution of the EBC-EBC interface has been defined as in Eq. (15), the integration of the incremental Eq. (11) can be numerically performed according to a uniform fibre discretisation of the EBC-EBC interface and the adjacent elements, as

depicted in Figure 6. The interface has been discretised into n_v cells centred at abscissae ξ_j, $j = 1,\ldots,n_v$ and, correspondingly, the two EBC connected macro-elements *r* and *s*, have been discretised according to n_v substrips. The adopted cell interval for the EBC-EBC interface is denoted with λ and each cell is endowed with an influence length over the adjacent EBC elements denoted as $l_f(\xi_j)$.

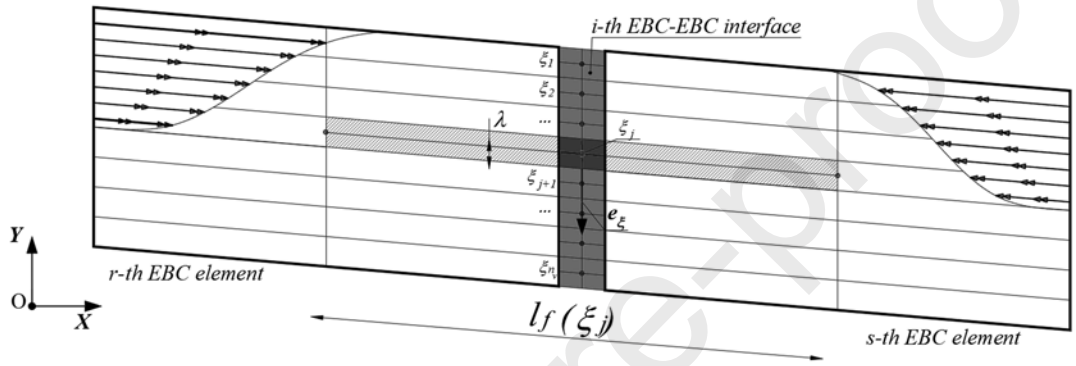

Figure 6. Fibre discretisation of the EBC-EBC interface in the case of non-rectangular geometry of the EBC elements

The discretised expression of the interface stiffness matrix proposed in Eq. (13) can now be formulated as follows:

$$\mathbf{K}_f = \sum_{j=1}^{n_v} \mathbf{A}^T \tilde{\mathbf{N}}_f^T(\xi_j)\, k_T(\xi_j)\, \tilde{\mathbf{N}}_f(\xi_j)\, \mathbf{A}\, \lambda \tag{16}$$

5. EBC-masonry interface mechanical behaviour

The crucial aspect of the EBC retrofitting technique is the interaction between the textile and the masonry support. The EBC-masonry interface represented in Figure 4, whose "ad

hoc" kinematic formulation has been proposed in subsection 3.2, is entitled to model the above interaction. An appropriate calibration of the mechanical non-linear behaviour of the interface, based on the phenomenological description of the EBC-masonry interaction, is pursued in this section.

A mechanical description of the above normal-flexural and tangential mechanisms is obtained by means of the formulation of the interface stiffness matrix and the calibration procedure of the relevant parameters apt to describe the non-linear constitutive laws, as reported in the following two subsections.

5.1. EBC-masonry interface stiffness matrix

The zero-thickness continuous EBC-masonry interfaces are characterised by a non-linear behaviour described by the incremental relationship between the increments of the internal tangential $\mathrm{d}\tau_\xi(\xi,\eta)$, $\mathrm{d}\tau_\eta(\xi,\eta)$, and normal $\mathrm{d}\sigma_\zeta(\xi,\eta)$ stresses along the two in-plane longitudinal ξ,η and the orthogonal ζ directions of the interface, respectively. The internal stress increments, collected in the vector $\mathrm{d}\boldsymbol{\sigma}^T(\xi,\eta)=\left[\mathrm{d}\tau_\xi(\xi,\eta)\quad \mathrm{d}\tau_\eta(\xi,\eta)\quad \mathrm{d}\sigma_\zeta(\xi,\eta)\right]$, can be expressed in terms of the relative displacement increment $\mathrm{d}\hat{\mathbf{u}}(\xi,\eta)$ of the vector $\hat{\mathbf{u}}(\xi,\eta)$, introduced in Eq. (10) where the subscripts *r,p* referred to the two connected EBC and masonry elements have been omitted for brevity, as follows:

$$\mathrm{d}\boldsymbol{\sigma}(\xi,\eta)=\mathbf{k}_T(\xi,\eta)\,\mathrm{d}\hat{\mathbf{u}}(\xi,\eta) \tag{17}$$

It has to be pointed out that the relationship introduced in Eq. (17) relates stress to displacement increments, rather than deformations, on account of the zero-thickness assumption for the interface. In Eq. (17), the 3x3 tangent stiffness distribution matrix $\mathbf{k}_T(\xi,\eta)$ of the EBC-masonry interface along the local coordinates ξ,η can be defined as follows:

$$\mathbf{k}_T(\xi)=\begin{bmatrix} k_{T_\xi}(\xi,\eta) & k_{T_{\xi\eta}}(\xi,\eta) & k_{T_{\xi\zeta}}(\xi,\eta) \\ k_{T_{\eta\xi}}(\xi,\eta) & k_{T_\eta}(\xi,\eta) & k_{T_{\eta\zeta}}(\xi,\eta) \\ k_{T_{\zeta\xi}}(\xi,\eta) & k_{T_{\zeta\eta}}(\xi,\eta) & k_{T_\zeta}(\xi,\eta) \end{bmatrix} \tag{18}$$

where, the subscripts ξ,η,ζ identify the two in-plane and the orthogonal directions of the generic EBC-masonry interface.

In view of Eq. (10), the force increment vector at the interface $\mathrm{d}\boldsymbol{\sigma}(\xi,\eta)$, given by Eq. (17), can be also expressed as function of the degrees of freedom increments of the corresponding adjacent elements, denoted as $\mathrm{d}\mathbf{d}_r, \mathrm{d}\mathbf{d}_p$, as follows:

$$\mathrm{d}\boldsymbol{\sigma}(\xi,\eta)=\mathbf{k}_T(\xi,\eta)\left[\mathbf{N}(\xi,\eta)\mathbf{A}_r\mathrm{d}\mathbf{d}_r-\mathbf{N}(\xi,\eta)\mathbf{A}_p\mathrm{d}\mathbf{d}_p\right] \tag{19}$$

By considering Eq. (19) and applying the principle of virtual work, the 13×13 tangent stiffness matrix of the EBC-masonry interface, dependent on the stiffness distribution $\mathbf{k}_T(\xi,\eta)$, is obtained as follows:

$$\mathbf{K}=\int_{A_{int}}\mathbf{A}^T\tilde{\mathbf{N}}^T(\xi,\eta)\mathbf{k}_T(\xi,\eta)\tilde{\mathbf{N}}(\xi,\eta)\mathbf{A}\,d\xi\,d\eta \tag{20}$$

being

$$\mathbf{A}=\begin{bmatrix}\mathbf{A}_r & \mathbf{0}\\ \mathbf{0} & \mathbf{A}_p\end{bmatrix};\qquad \tilde{\mathbf{N}}(\xi,\eta)=\begin{bmatrix}\mathbf{N}(\xi,\eta) & -\mathbf{N}(\xi,\eta)\end{bmatrix} \tag{21}$$

The generic EBC-masonry interface, through the above stiffness matrix definition, is representative of the elastic/inelastic normal and tangential behaviours of adjacent portions of masonry and EBC textile, considered as an equivalent homogeneous medium.

The integration in Eq. (20) providing the tangent stiffness matrix $\mathbf{K}$, can be numerically performed according to the discretisation of the EBC-masonry interface depicted in **Error! Reference source not found.**. The interface is here discretised into $n_\xi \times n_\eta$ cells centred at points (ξ_i,η_j) each characterised by the area A_{ij}, $i=1,\dots,n_\xi$, $j=1,\dots,n_\eta$, and the EBC-masonry stiffness matrix defined in Eq. (20) may be evaluated according to the following discretised expression:

$$\mathbf{K}=\sum_{i=1}^{n_\xi}\sum_{j=1}^{n_\eta}\mathbf{A}^T\tilde{\mathbf{N}}_f^T\left(\xi_i,\eta_j\right)\mathbf{k}_T\left(\xi_i,\eta_j\right)\tilde{\mathbf{N}}_f\left(\xi_i,\eta_j\right)\mathbf{A}\,A_{ij} \tag{22}$$

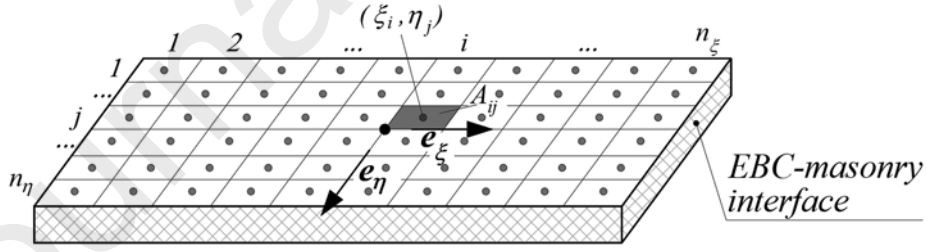

Figure 7. Cell discretisation of the EBC-masonry interface

In the next subsection, the relevant procedure for the calibration of the components of the interface stiffness matrix will be presented in detail for a specific constitutive behaviour. However, it must be borne in mind that the proposed macro-element modelling procedure can accommodate any non-linear constitutive law to model the interaction between the EBC textile and the masonry support, also in view of the type of reinforcement at hand.

5.2. Non-linear constitutive laws and stiffness calibration of the EBC-masonry interface

In this subsection, the strategy for a straightforward calibration of the EBC-masonry interface stiffness distribution is presented. The proposed calibration procedure, without loss of generality, is based on a choice of the non-linear constitutive law governing the EBC-masonry interaction.

The EBC-masonry plane interface is responsible of governing the non-linear behaviour associated with a progressive detachment of the EBC textile from the masonry due to the action of normal tensile stresses as well as the progressive transfer of the tangential force between the EBC strips and the masonry support.

Aiming at offering a simplified calibration procedure of the interface constitutive behaviour, a partial decoupling of the normal tensile/compressive stress from the shear stresses, analogously to the constitutive laws presented in [70] for the case of r/c cross sections in accordance to a fibre approach, is considered. Specifically, the shear mode behaviour is ruled by the stress resultant, accounting for both shear components, and depends on the normal stress as a state parameter. The adopted laws are formulated in what follows

as stress-displacement curves, accounting for the fracture energy, leading to a limited mesh dependency. Plastic strains have the same orientation of the normal stress for mode I, and of the shear stress resultant for mode II and not orthogonal to the yielding domain (non-associative flow rule). In accordance to the latter assumptions in the following sub-sections the constitutive behaviour related to the normal tensile/compressive stress and to the shear stress are presented and a simplified calibration of the tangent stiffness matrix of the interface is discussed.

5.2.1 Non-linear modelling of EBC-*masonry interface normal stresses*

Characterisation of the behaviour associated with normal tensile/compressive stresses σ_ζ in the direction orthogonal to the EBC-masonry interface is here provided. A specific non-linear constitutive law decoupled from the shear stresses τ_ξ, τ_η that allows an independent calibration of the tangent stiffness component $k_{T_\zeta}(\xi,\eta)$, by assuming null the coupling terms $k_{T_{\xi\zeta}}(\xi,\eta), k_{T_{\zeta\xi}}(\xi,\eta), k_{T_{\eta\zeta}}(\xi,\eta), k_{T_{\zeta\eta}}(\xi,\eta)$, is formulated. Nevertheless, the influence of the normal stress σ_ζ on the bond-slip phenomenon related to the shear stresses τ_ξ, τ_η will be accounted for as shown in the next subsection.

The behaviour under consideration is governed by the elasto-plastic constitutive law represented in Figure 8 in terms of normal stress σ_ζ and relative displacement of the interface $\hat{w}_{r,p}(\xi,\eta)$. The behaviour depicted in Figure 8 is elastic in traction (compression) up to the tensile (compressive) elastic limit point $\sigma_t, \hat{w}_t$ ($\sigma_c, \hat{w}_c$) characterised by the elastic

stiffness k_n both in traction and compression. The tensile (compressive) elastic range is followed by a descending linear softening branch up to a limit relative displacement $\hat{w}_{u,t}$ ($\hat{w}_{u,c}$) attained upon development of a corresponding tensile (compressive) fracture energy level G_t (G_c), i.e. $\hat{w}_{u,t} = 2G_t/\sigma_t + \hat{w}_t$ ($\hat{w}_{u,c} = 2G_c/\sigma_c + \hat{w}_c$). The softening branches in traction and compression are hence characterised by the tangent stiffness $k_t = -\sigma_t/\left(\hat{w}_{u,t} - \hat{w}_t\right)$, $k_c = -\sigma_c/\left(\hat{w}_{u,c} - \hat{w}_c\right)$, respectively.

In view of the above-described constitutive behaviour along the ζ axis across the entire interface field, the components of the tangent stiffness distribution in Eq. (18) are defined as follows:

$$
\begin{aligned}
&k_{T_\zeta}(\xi,\eta) = k_n \quad \text{for} \quad -\hat{w}_c \le \hat{w} < \hat{w}_t \\
&k_{T_\zeta}(\xi,\eta) = k_t \quad \text{for} \quad \hat{w}_t \le \hat{w} < \hat{w}_{u,t}, \quad d\hat{w} > 0 \\
&k_{T_\zeta}(\xi,\eta) = k_c \quad \text{for} \quad -\hat{w}_{u,c} \le \hat{w} < -\hat{w}_c, \quad d\hat{w} < 0 \\
&k_{T_\zeta}(\xi,\eta) = 0 \quad \text{for} \quad \hat{w} \le -\hat{w}_{u,c} \quad \text{or} \quad \hat{w} \ge \hat{w}_{u,t} \\
&k_{T_{\xi\zeta}}(\xi,\eta) = k_{T_{\zeta\xi}}(\xi,\eta) = k_{T_{\eta\zeta}}(\xi,\eta) = k_{T_{\zeta\eta}}(\xi,\eta) = 0
\end{aligned}
\tag{23}
$$

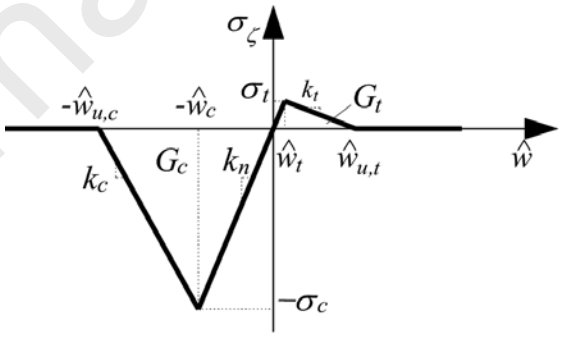

Figure 8. Debonding constitutive law

The above constitutive behaviour is considered to simulate the possibility of crushing of the masonry support, or the mortar interface in case of FRCM, as well as the detachment of the EBC element from the masonry substrate due to the achievement of ultimate tensile stress. The relevant parameters characterising the behaviour in tension can be calibrated in accordance with specific pull off tests. On the other hand, the compression parameters could be inferred by the masonry properties for the case of FRP, while the mortar parameters should also be accounted for in the case of FRCM. However, the attainment of the limit elastic stress in compression is not generally observed.

5.2.2 Bond-slip constitutive law associated with shear stresses

Characterisation of the behaviour associated with shear stresses acting between the EBC textile and the masonry support allows the calibration of the tangent stiffness components $k_{T_\xi}(\xi,\eta), k_{T_\eta}(\xi,\eta), k_{T_{\xi\eta}}(\xi,\eta), k_{T_{\eta\xi}}(\xi,\eta)$ of the stiffness matrix in Eq. (18) characterising the two in-plane directions parallel to the EBC-masonry interface.

The numerical simulation of the bond-slip failure mechanism of a EBC masonry element appears a very difficult task and not many papers have been devoted to a proper study of the phenomenon [29]. On the contrary, in the literature, many authors [39] and codes [21] often treat this phenomenon by considering perfect adherence between the masonry and the EBC material and by assigning to the latter a fictitious tensile strength, to be calculated mainly according to the properties of the fibres and of the masonry support. However, the physical phenomenon is characterized by a progressive transfer of the tangential action between the

reinforcements and the masonry, which leads to the definition of the so-called optimal bond length, that is the required length of the reinforcement strips to properly activate all the tangential strength resources in the EBC-masonry interface. To this regard, it is clear that a model based on a fictitious EBC tensile strength considers either the debonding stress or the tensile strength of the composite and is not able to identify the progressive transfer of tangential forces along the EBC-masonry interfaces. Only a few proposals in the literature are devoted to a proper identification of a bond-slip law, considering FRP-concrete systems [22],[23] and strengthened masonry [25]-[28]. The interface element described in this subsection belongs to this latter framework. In particular, an effective bi-directional tangential modelling of the cohesive-friction type ruling the non-linear behaviour of the EBC-masonry interface is introduced in what follows.

It is worth mentioning that the proposed model can be ideal when the bond-slip behaviour can occur in accordance to a single failure mode such as, for instance, the case of FRP strengthening techniques. On the other hand, the different possible tangential collapse mechanisms characterising the case of FRCM reinforcement, are condensed in the model in a single constitutive behaviour.

Without loss of generality, a Mohr-Coulomb approach is assumed adopting a yield dominium Φ across the area A_{int} of the EBC-masonry interface as follows:

$$\Phi(\tau,\sigma_\zeta)=\sqrt{\tau_\xi^2+\tau_\eta^2}-c+\mu\cdot\sigma_\zeta+c\,\delta=0 \qquad \text{with} \qquad \begin{cases}\delta=\dfrac{W_p}{G_{sl}} & \text{for } W_p\le G_d\\ \delta=1 & \text{for } W_p>G_d\end{cases} \tag{24}$$

where $\sqrt{\tau_\xi^2+\tau_\eta^2}=\tau$ represents the modulus of the resultant shear stress vector $\boldsymbol{\tau}=\tau_\xi\mathbf{e}_\xi+\tau_\eta\mathbf{e}_\eta$ and where the mechanical parameters cohesion c and coupling factor μ have been introduced. The last term in Eq. (24) has been introduced to account for a linear isotropic softening shrinkage dependent on the development of the plastic work W_p up to the achievement of the delamination fracture energy G_d. The yield dominium in Eq.(24) is represented in Figure 9a. The behaviour is assumed elastic when the shear stress resultant lies inside the dominium ($\Phi(\tau,\sigma_\zeta)<0$) while it is plastic otherwise. Plastic slip s is assumed to develop in the direction parallel to the shear stress resultant vector at the beginning of each step of the non-linear analysis implying the adoption of a forward Euler integration rule. The latter assumption corresponds to a non-associated flow rule with a plastic potential defined by a circle centred at the origin in the τ_ξ,τ_η stress space and represented by the direction parallel to the τ axis in the τ,σ_ζ plane in Figure 9a.

For simplicity reasons only, the variable σ_ζ in Eq. (24) is treated as a parameter, rather than a proper variable, whose value is updated when equilibrium at the interface level is enforced. As a consequence, in order to account for the influence of the normal stress on the tangential behaviour, the yield dominium can be treated as a single variable yield function indicated as $\Phi(\tau;\sigma_\zeta)$ in what follows. In accordance with the latter reasoning, the non-linear shear behaviour of the interface is described by a bi-linear constitutive law undergoing softening

descending branches dependent on the normal stress σ_ζ. The latter constitutive law is represented in Figure 9b in terms of shear stress $\tau = \sqrt{\tau_\xi^2 + \tau_\eta^2}$ and relative displacement $\hat{u}_R = \sqrt{\hat{u}^2 + \hat{v}^2}$ resultant moduli in the ξ, η plane of the interface.

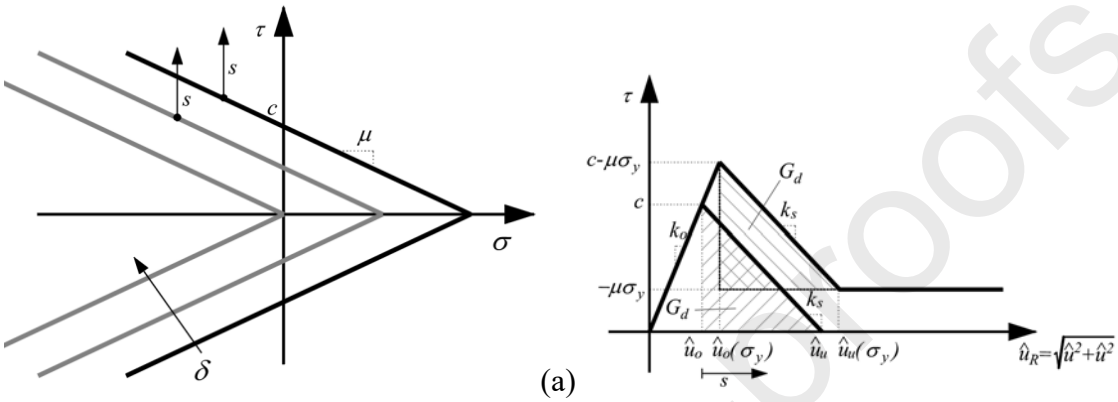

Figure 9. Bond slip constitutive law of the EBC-masonry interface: (a) Mohr-Coulomb yield domain; (b) tangential stress versus tangential displacement for different values of normal stress

The elastic branch represented in Figure 9b is characterised by a shear elastic stiffness k_o, and the elastic limit shear stress value $\tau_o(\sigma_\zeta) = c - \mu\sigma_\zeta$, correspondent to the displacement value $\hat{u}_o(\sigma_\zeta) = \tau_o(\sigma_\zeta)/k_o$. The softening behaviour is characterised by a constant negative stiffness $k_s = -c/\left[\hat{u}_u(\sigma_\zeta) - \hat{u}_o(\sigma_\zeta)\right]$, where $\hat{u}_u(\sigma_\zeta)$ is the ultimate displacement attained upon development of the corresponding mode II fracture energy G_d evaluated as follows:

$$\hat{u}_u(\sigma_\zeta) = 2\frac{G_d}{c} + \hat{u}_o(\sigma_\zeta) \tag{25}$$

The plateau in Figure 9b corresponds to the residual tangential strength of the EBC on the masonry support depending on the friction action and related to the acting normal stress. An estimation of such parameter can be obtained through bond-slip tests on a flat support where a constant normal action is applied on the EBC, or by bond-slip tests considering a curved support.

The stiffness k_s, characterising the softening behaviour, can be inferred by Eq. (25) as $k_s = -c^2/2G_{sl}$. The components of the interface stiffness matrix are derived by the above constitutive law where, in particular, the coupling terms $k_{T_{\xi\eta}}(\xi,\eta), k_{T_{\eta\xi}}(\xi,\eta)$ are neglected, as follows:

$$\begin{aligned}
&k_{T_\xi}(\xi,\eta) = k_{T_\eta}(\xi,\eta) = k_o \quad \text{for} \quad \Phi(\tau;\sigma_\zeta) < 0 \quad \text{or} \quad \Phi(\tau;\sigma_\zeta) = 0 \quad \text{and} \quad \mathrm{d}\Phi(\tau;\sigma_\zeta) \le 0 \\
&k_{T_\xi}(\xi,\eta) = k_{T_\eta}(\xi,\eta) = k_s \quad \text{for} \quad \Phi(\tau;\sigma_\zeta) = 0 \quad \text{and} \quad \mathrm{d}\Phi(\tau;\sigma_\zeta) > 0 \\
&k_{T_\xi}(\xi,\eta) = k_{T_\eta}(\xi,\eta) = 0 \quad \text{for} \quad \hat{u}_R = \sqrt{\hat{u}^2 + \hat{v}^2} \ge \hat{u}_u(\sigma_\zeta) \\
&k_{T_{\xi\eta}}(\xi,\eta) = k_{T_{\eta\xi}}(\xi,\eta) = 0
\end{aligned} \tag{26}$$

It has to be remarked that the effort produced in the formulation of the proposed model aims at devising an approach able to conjugate the need of an adequate and reliable modelling of the complex interaction at hand with the aspiration to keep low the computational cost of the simulations and simple the interpretation of the outcome of the numerical analyses.

The latter results was pursued in accordance to two main aspects:

i) keeping the size of the problem as low as possible by considering the essential degrees of freedom in the elements

ii) adopting uniaxial constitutive laws.

With regard to the second aspect, the complexity of the problem would rigorously imply the adoption of coupled multi-axial constitutive laws; however, there are quite a few proposal in the literature of constitutive behaviours for externally bonded composites applied to masonry structures which fall within the uniaxial behaviours (e.g. [39]). In this regard, in the adopted procedure, although based on uniaxial constitutive laws, a proper three-dimensional behaviour of the models is retrieved considering the detailed discretisation by means of the fibre approach of the interfaces. The fibre approach proved to be effective in the case of reinforced concrete structures [65], considering that all the uni-axial fibres are distributed over the integration domain. In any case, when the adoption of a multi-axial constitutive behaviour seems to play a more relevant role (e.g. the tangential behaviour of the EBC-masonry interface) a biaxial behaviour is assumed, also able to account for the interaction with normal force acting on the interface although treated in a simplified manner.

It is worth to note the proposed model, rather than aiming at a refined approach able to obtain a micro-modelling of the response, is devoted to a discrete macro-modelling strategy able to describe the effect of composite reinforcement on entire structural elements.

All the adopted constitutive laws and the subsequent calibration of the model are energy-based and the proposed approach was compared, at least for unreinforced curved masonry structures, with more refined approaches [71]; in addition, comparisons of the results obtained

by means of the DMEM both at the macro- and at the meso-scale in the case of unreinforced masonry structures are also available [64].

6. Model validation on single shear lap tests

The validation of the proposed model has been performed by means of numerical simulations of an experimental campaign led at the University of Minho [50] and a consequent thorough comparison. Precisely, a complete numerical simulation aiming at considering single shear lap tests on Glass Fiber Reinforced Polymer (GFRP) applied on a masonry support will be presented and discussed in what follows.

In the experimental campaign conducted at the University of Minho [50] tensile tests on the dry glass fibres (employed in the GFRP) with equivalent thickness 0.149 mm were conducted, leading to the definition of the material properties summarized in Table 1.

Table 1. Adopted mechanical properties for the GFRP reinforcements

Material	E_f [MPa]	σ_y [MPa]	ε_y [%]	t_f [mm]
GFRP	45000	1473	3.19	0.149

In order to validate the capability of the proposed model to describe the progressive transfer of the tangential forces along the EBC-masonry interface and its capability of predicting mode II failure mode, bond-slip tests are reproduced. The reference specimen, identified by G150R, is composed of a GFRP strip applied with epoxy resin, with a 25 mm width and 150 mm length, glued onto the top surface of a masonry prism with length 260 mm, width 130 mm and height 100 mm.

Four further specimens have been considered in the numerical simulations in order to investigate the effects of the anchorage length (l_a) and of the radius (R) of the masonry support:

- G100R: flat surface and l_a =100 mm;
- G200R: flat surface and l_a =200 mm;
- G150X: convex surface of the masonry support with R= 1262.5 mm, and l_a =150mm;
- G150E: concave surface of the masonry support with R= 1262.5 mm, and l_a =150mm.

The mechanical properties that characterise the bond-slip behaviour of the EBC-masonry interfaces, are taken from [50] (and reported in Table 2), where also detailed analyses by finite element models have been performed, considering a composite interface model formulated within the framework of plasticity, which includes a tension cut-off for mode I, the Coulomb friction envelope for mode II, and a cap mode for compressive failure, according to [72]. The adopted mesh size, both for the FRP and the masonry elements, is 1 cm. Masonry for this application is assumed to be elastic with Young's and shear moduli equal to 2040 MPa and 850 MPa, respectively.

Table 2. Adopted bond slip mechanical properties for the masonry-FRP reinforcement interfaces

k_n [N/mm^3]	σ_t [MPa]	G_t [N/mm]	σ_c [MPa]	G_c [N/mm]	k_s [N/mm^3]	c [MPa]	μ	G_d [N/mm]
48	0.44	0.15	7.8	90	20	1.3	0.75	2.5

Figure 10 shows the numerical curves for the G150R specimen, in terms of external force (F) and displacement at the loaded point (u), compared with the envelope of the experimental

data (grey area). In the same Figure 10 the numerical results obtained in [50] are also reported.

The curve obtained by the proposed model is in good agreement both with the finite element curve and with the experimental envelope. Limited difference between the results of the FEM and the proposed discrete model can be observed in terms of ultimate load though both lie in the experimental envelope grey zone. In particular, the difference between the two models in terms of ultimate force is about 13%. Regarding to displacement capacity (displacement at ultimate load) the two models are in a very good agreement.

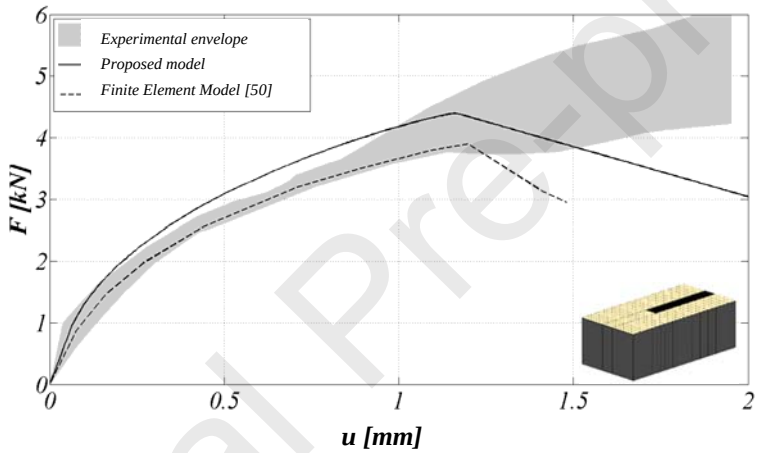

Figure 10. Bond-slip tests on flat surface masonry prism; comparison between numerical curves and experimental envelope (G150R).

Figure 11 reports the numerical responses, compared with the experimental data, relative to the flat specimens with different anchorage lengths G100R (Figure 11a) and G200R (Figure 11b), while Figure 12 is relative to the curved specimens G150E (Figure 12a) and G150X (Figure 12b).

In all the investigated cases the proposed model is able to simulate experimental tests with a good accuracy. Larger discrepancies can be observed in the case of concave surface (Figure 12a); however, also for this case a satisfactory prevision of the ultimate experimental load is obtained. It has to be noted that the numerical results provided by the detailed finite element model and the proposed model are coherent to each other in all the investigated cases, both in terms of ultimate load and capacity displacement.

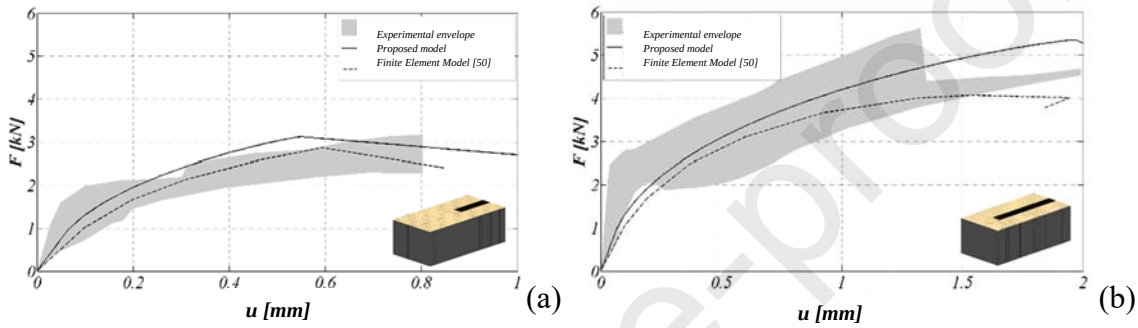

Figure 11. Influence of the anchorage length on the Bond-slip response; (a) L=100mm (G100R); (b) L=200mm (G200R).

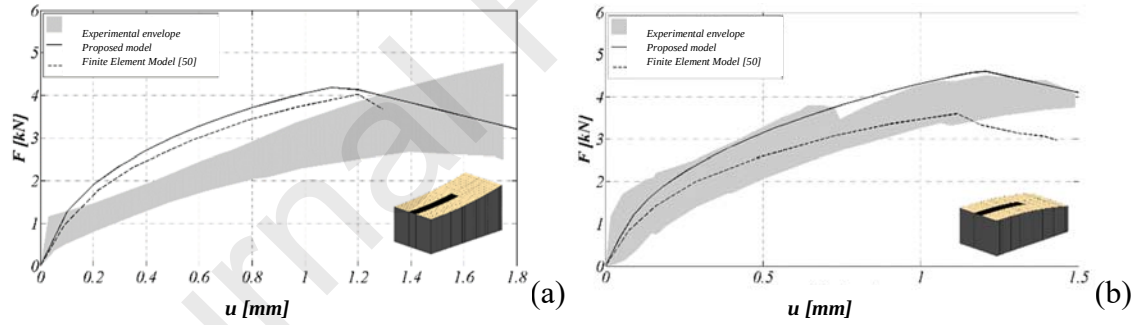

Figure 12. Bond-slip response on curved support with R=1262.5 mm; (a) concave surface (G150E); (b) convex surface (G150X).

A further comparison between numerical results and experimental outcomes can be done in terms of longitudinal stresses along the length of the fibre reinforced strip which were

experimentally measured by means of strain gauges for different values of the applied external load (25% and 75% of the peak load). Precisely, in Figure 13 the longitudinal stress obtained with the proposed model as well as with numerical simulations conducted in [50] are compared with the experimental measurements. The agreement between experimental data and numerical simulations seems to be very good, thus demonstrating how the proposed model is able to catch the real stress distribution and evolution along the fibre reinforced strips.

Based on the accuracy of the proposed model shown by the comparison with experimental results further aspects on the interaction between the fibre reinforced textile and the masonry support are investigated in what follows.

In order to better highlight the influence of the anchorage length on the accuracy proposed model, in Figure 14a, the numerical results obtained with the proposed model relative to three of the considered specimens have been compared (G100R, G150R, G200R). The results show how the peak load increases with the anchorage length, till getting very close to the force inducing tensile rupture of the fibre reinforced strips implying a sudden reduction of the carrying capacity without reaching the so-called effective bond length. Indeed, in [50] the author states that «If the anchorage length is large (200 mm) before the anchorage slides, the FRP strip fails in tension». For the latter reason the effective bond length doesn't seem to be a significant parameter for the case at hand. In Figure 14b the superposition of curves relative to the proposed macro-model for all the analysed curvatures, is reported. It can be observed,

in presence of a coupling factor, an increment of the ultimate load for the convex model (G150X) and a decrement for the concave model (G150E) with respect to the flat model (G150R) because of the influence of the normal stress, in the direction orthogonal to the layer reinforcement, on the shear strength.

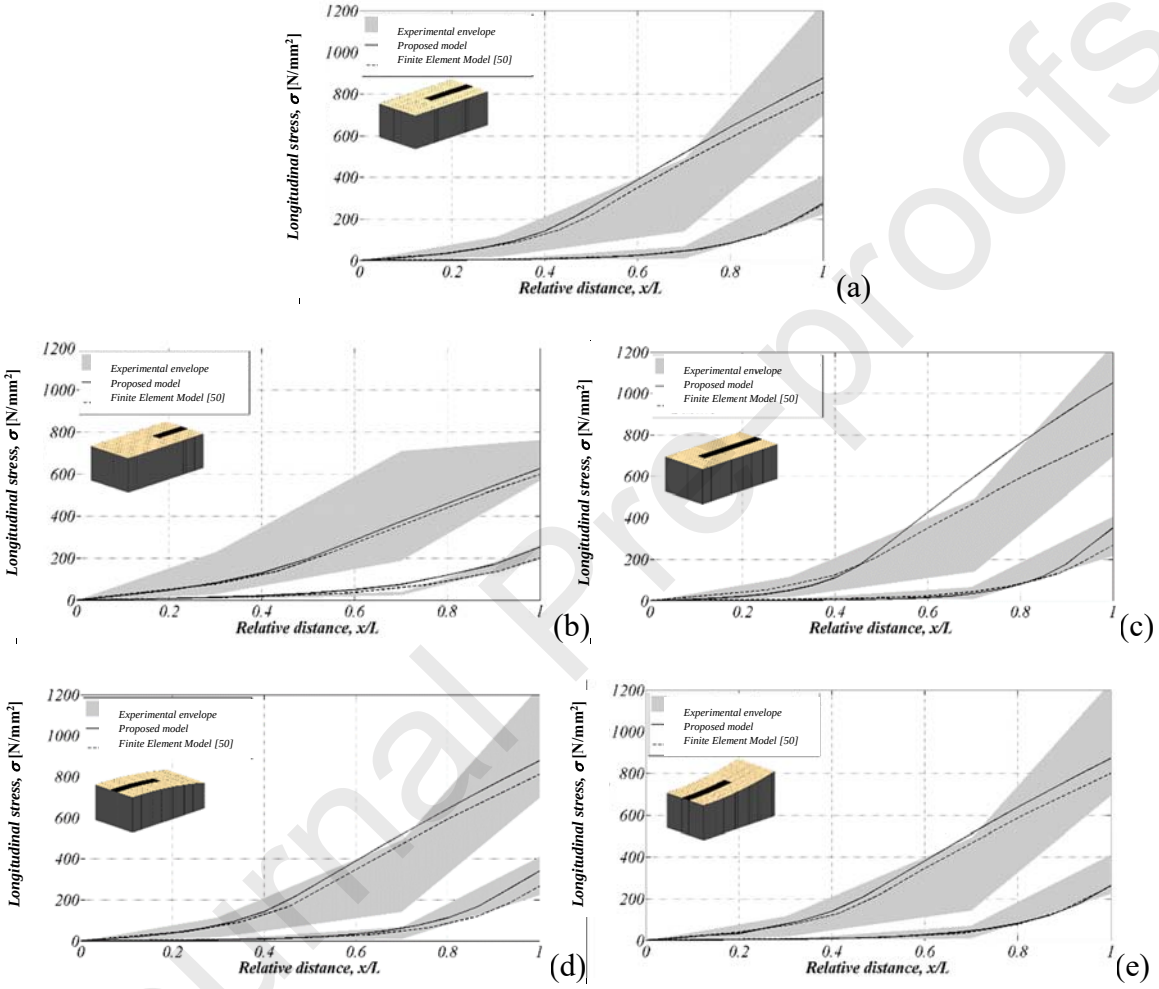

Figure 13. Comparison among the delamination tests in terms of longitudinal stress along the strips for different values of the applied external load: (a) G150R, (b) G100R, (c) G200R, (d) G150X, (e) G150E.

The influence of the coupling factor is better shown in Figure 15 where the peak load relative for three masonry supports (flat, concave and convex) is reported as a function of μ.

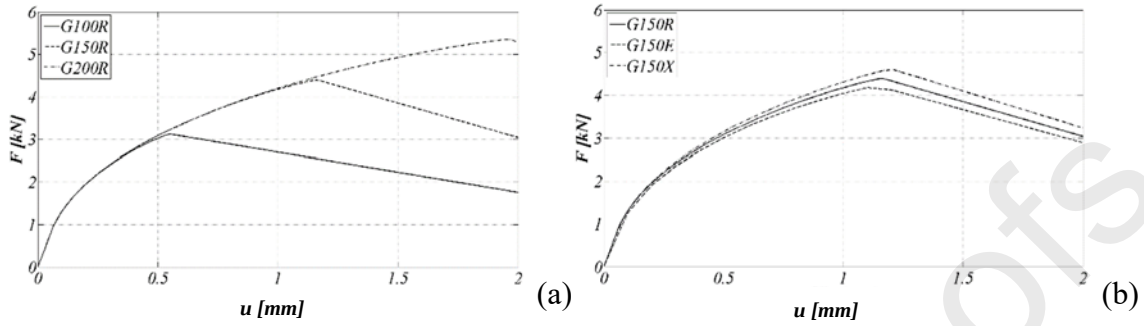

Figure 14. Comparison among the delamination tests: (a) effect of the anchorage length and (b) effect of the curvature of the masonry support surface.

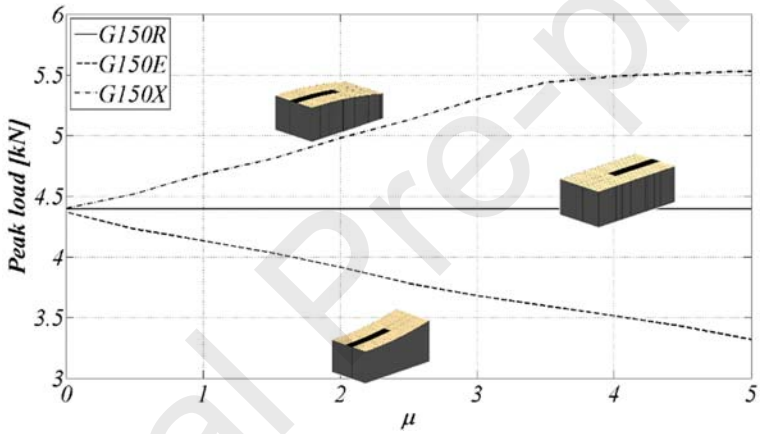

Figure 15. Influence of the coupling factor on the ultimate strength.

In Figure 15 it can be observed that for the convex model the ultimate load increases with the coupling factor μ up to the value about $\mu = 3.5$ corresponding to an overstrength of about 40% with respect to the uncoupled condition. Above that point the ultimate load is governed by the rupture of the fibre reinforced strips. On the other hand, for the concave model the influence of the coupling factor μ leads to a continuously decreasing trend of the

capacity strength. In Figure 16 the numerical responses for the cases of the two curved masonry supports, for the values $\mu = 0, 2, 4$, are reported. It can be observed how the ultimate displacement decreases with the coupling factor for the concave support and on the contrary it increases for the convex support unless the tensile collapse of the fibre reinforced textile occurs as shown by the sudden drop of the curve for $\mu = 4$.

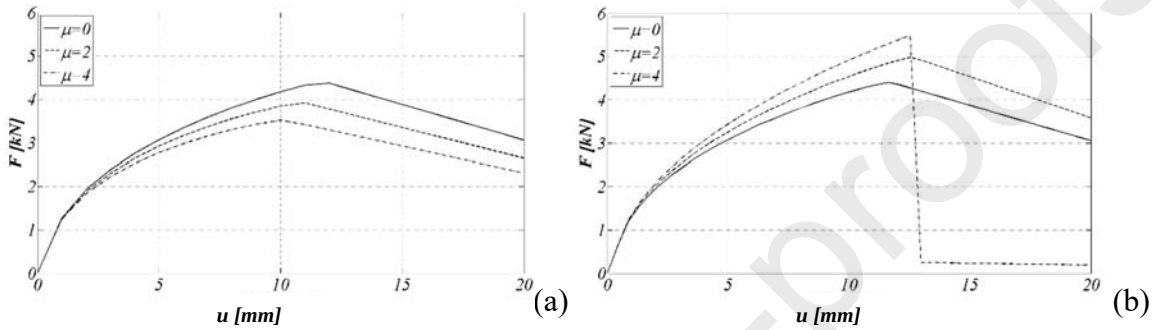

Figure 16. Load-displacement curves for several values of the coupling factor: (a) concave surface (G150E); (b) convex surface (G150X).

7. Validation of the model against out-of-plane loaded reinforced masonry walls

This section presents a validation of the proposed approach with respect to out-of-plane loaded reinforced masonry panels. The presented application is significant for two main reasons:

i) the prevention of out-of-plane mechanisms in masonry walls is a common scope of the application of fibre-reinforced textiles on masonry structures;

ii) the considered application is made with a Basalt Fibre Reinforced Cementitious Mortar (BFRCM) technique, thus demonstrating the possibility to apply the model also in presence of different techniques.

There is a wide literature on the flexural experimental behaviour of out-of-plane loaded masonry walls reinforced with composites. A comprehensive comparative study on the field can be found in [73]. Among the studies therein collected, a case treated more in detail in [49] and object of experimental test, characterising the efficacy of the BFRCM technique to improve the out-of-plane response of masonry wallets, has been selected. Precisely, after a proper component characterization (masonry, basalt fibre mesh reinforcement), unreinforced and reinforced masonry wallets are subjected to three-point (line) flexural loading.

To characterise the masonry, made of solid clay bricks and cement-sand mortar, masonry prisms were subjected to uniaxial loading. The experimental stress-strain curves envelope of the six tests is reported in Figure 17 with a grey band, subsequently employed to calibrate the masonry mechanical properties on the basis of the value of the average compressive strength and assuming a parabolic law in compression, represented with the solid line in Figure 17. The relevant data are reported in Table 3.

In [49] four out-of-plane bending tests on unreinforced wallets were also executed, and the corresponding results in terms of load-displacement curves envelope are reported in Figure 18a with the grey band. The latter results are here exploited to calibrate the tensile properties of the masonry. The relevant results are reported with a solid line in Figure 18a by adopting tensile strength and fracture energy reported in Table 3, in accordance to a proper fitting of the experimental tests. An exponential softening in tension was assumed, whereas the diagonal and sliding shear non-linear failure modes were inhibited.

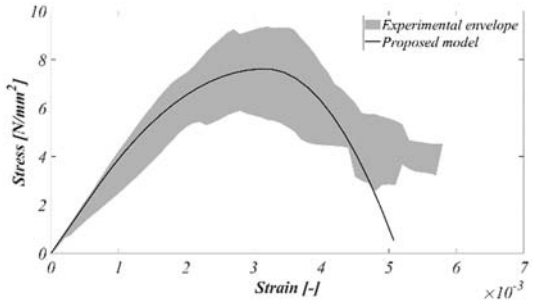

Figure 17. Compressive strain-stress curve adopted for the uniaxial behaviour of masonry.

Table 3. Masonry mechanical properties

E [MPa]	σ_t [MPa]	G_t [N/mm]	σ_c [MPa]	G_c [N/mm]	G [MPa]	w [kN/m^3]
4000	0.12	0.03	7.62	10	1600	18

For the reinforcement a 25 mm basalt fibre grid embedded in a cement mortar layer has been considered. The equivalent properties of the employed BFRCM reinforcement are summarized in Table 4. Since no nominal thickness for the textile was provided in the description of the experimental tests, but rather mechanical properties per unit length were given, the nominal thickness is a free parameter of the model which was arbitrarily set equal to 0.01 mm; the corresponding limit tensile strength σ_y was related to the tensile strength of the grid (66 kN/m) divided by the nominal thickness, whereas the Young's modulus E was obtained dividing the tensile strength σ_y by ultimate strain ε_u equal to 0.0114. Although it could be preferable to adopt more sophisticated constitutive laws to simulate the axial behaviour of BFRCM, a simple elastic-brittle constitutive law was assumed for the reinforcement package. Regarding the BFRCM-masonry interface characterization, no specific tests were conducted, therefore the normal behaviour is considered elastic and the

adopted properties were conveniently chosen within typical range for the reinforcement typology [74].

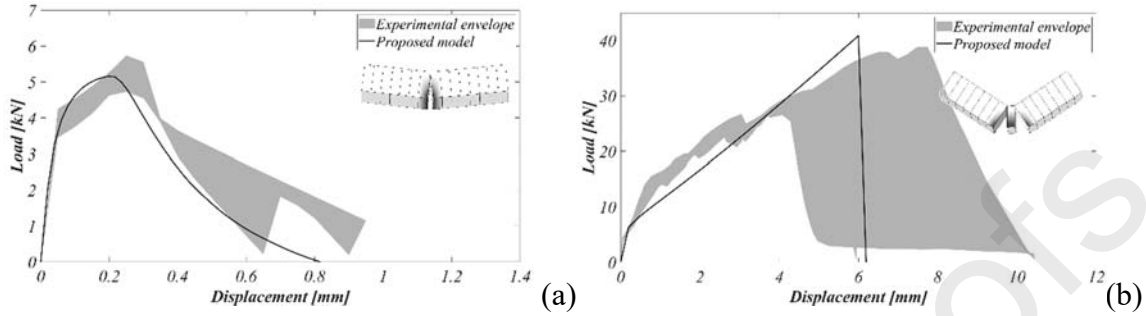

Figure 18. Load-displacement curves of the (a) unreinforced and (b) strengthened masonry walls.

Table 4. Mechanical properties adopted for the BFRCM

Uniaxial EBC element properties		EBC-masonry interface properties								
E [MPa]	σ_y [MPa]	k_n [N/mm^3]	σ_t [MPa]	G_t [N/mm]	σ_c [MPa]	G_c [N/mm]	k_s [N/mm^3]	c [MPa]	μ	G_d [N/mm]
57895	660	48	-	-	-	-	75	0.75	0	0.26

The comparison in terms of load-displacement curve, considering the envelope of the four experimental tests with a grey band, and the numerical simulation, is reported in Figure 18b, showing a very good agreement in terms initial stiffness peak load and brittle behaviour. In the same figure, the collapse mechanism, involving the rupture of the reinforcement in the middle part of the masonry wall, consistent with the outcome of the experimental tests, is also shown.

8. Model validation on circular arches

In this section the proposed macro-element model is validated by means of numerical simulations relative to a set of circular masonry arches tested at the university of Minho [50],[51] under unreinforced and GFRP reinforcement arrangements according to different layouts. The arch width is 450 mm, the radius is 770 mm, the inner span 1500 mm and the thickness is 50 mm. Five different configurations for the arch have been considered:

- US - unstrengthened arch, Figure 19a;
- LS – locally strengthened arch by means of 4 strips at the extrados (4x70 mm width GFRP strips) and 2 strips at the intrados (2x80 mm width GFRP strips) whose length is $p/4$ (p is the perimeter of the arch), as better shown in Figure 19b;
- CSEa - arch strengthened at the extrados with 2x50 mm width GFRP continuous strips, Figure 19c;
- CSEb - arch strengthened at the extrados with 2x80 mm width GFRP continuous strips, Figure 19d;
- CSI - arch strengthened at the intrados with 2x50 mm width GFRP continuous strips, Figure 19e.

All the arch configurations were subjected to the same load scenario, that is a concentrated vertical load applied at a quarter of the arch span. Further details on the test layout can be found in [50][51].

Lateral view | Plan view

US

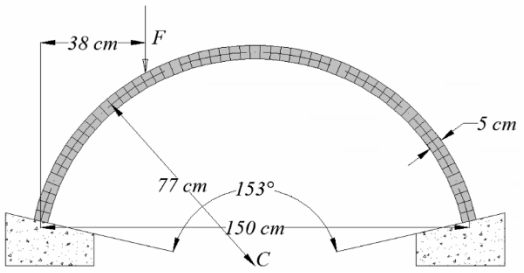

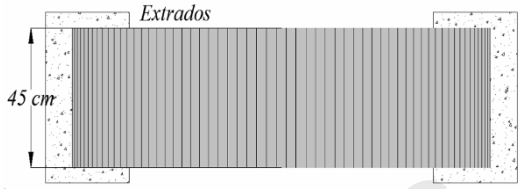

LS

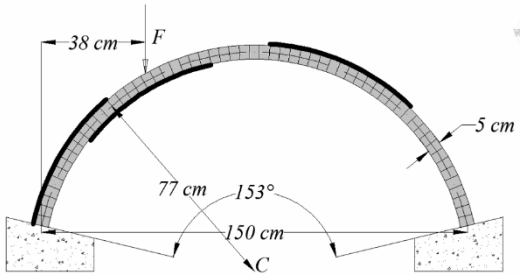

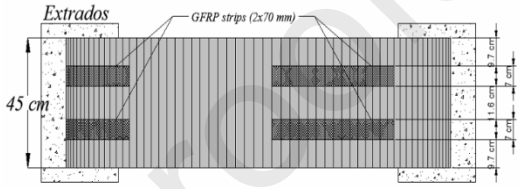

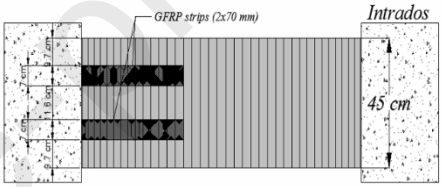

CSEa

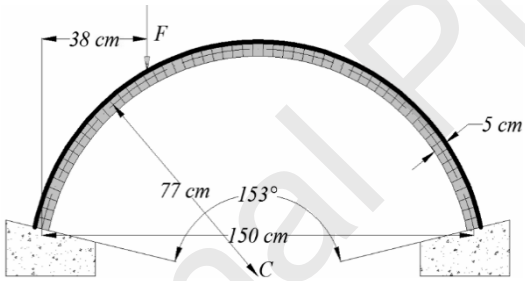

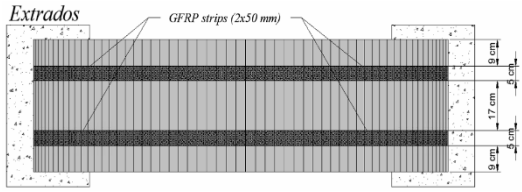

CSEb

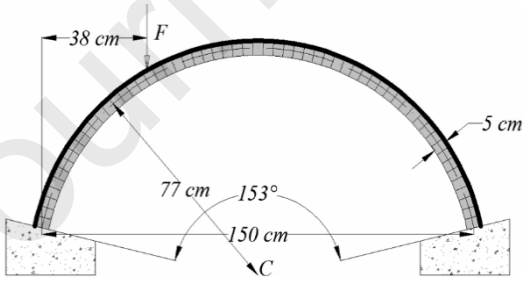

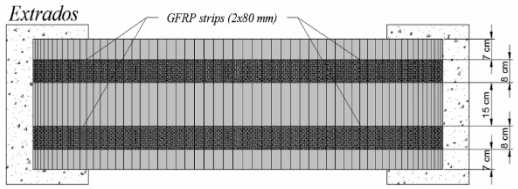

CSI

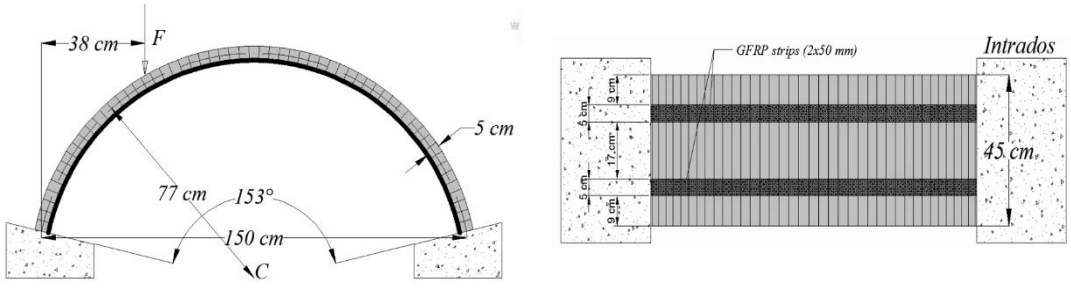

Figure 19. Experimental layout for the arches: (a) US, (b) LS, (c) CSEa, (d) CSEb, (e) CSI.

A homogenized continuous material is considered for the masonry support. The mechanical properties adopted in the analyses are reported in Table 5 where G_{sl} indicates the fracture energy relative to the sliding mechanism. The mechanical parameters that govern the bond-slip and normal stress interaction between masonry and GFRP reinforcements, are reported in Table 6.

Table 5. Mechanical properties adopted for the masonry support

E [MPa]	σ_t [MPa]	G_t [N/mm]	σ_c [MPa]	G_c [N/mm]	G [MPa]	c [MPa]	μ	G_{sl} [N/mm]	w [kN/m^3]
2040	0.28	0.02	7.8	90	850	0.28	0.4	0.1	15

Table 6. Mechanical properties adopted for the EBC strip-masonry interface

k_n [N/mm^3]	σ_t [MPa]	G_t [N/mm]	σ_c [MPa]	G_c [N/mm]	k_s [N/mm^3]	c [MPa]	μ	G_d [N/mm]
48	0.44	0.15	7.8	90	20	0.65	0.75	0.25

The numerical models were discretised consistently with the units' arrangement of the experimental specimens. For computational convenience, due to the symmetry of the specimens and of the reinforcements, although in the experimental tests the strips were always applied in pairs, in the numerical model single strips with double width were considered. Specifically, the number of masonry and EBC elements adopted in the models

and the corresponding computational demand in terms of degrees of freedom, are reported in Table 7.

The non-linear behaviour of the analysed arch configurations is expressed in terms of:

i) capacity curve, i.e. the external applied force versus the vertical displacement of the force application point, reporting the opening sequence of the plastic hinges;

ii) collapse mechanisms, together with a damage map in terms of plastic strain;

iii) characterization of the plastic hinges, identifying typology (flexural or shear) location (intrados or extrados) and position in terms of distance from the left end of the arch.

Table 7. Number of elements and degrees of freedom adopted for the numerical modelling

Arch	Masonry discrete elements	EBC discrete elements	Degrees of freedom
US	59	0	413
LS	59	44	677
CSEa	59	59	767
CSEb	59	59	767
CSI	59	59	767

The results are compared with the experimental tests, but also with the numerical simulations reported in [50] and, for some of the analysed cases, in [39]. In the latter paper, the strength of the equivalent rods is selected as the minimum strength among all those leading to possible failure modes which involve the FRP reinforcement; in particular, the results reported in the applications with regard to the latter approach are relative to the *Set III* strategy, according to the terminology adopted in the referenced paper [39].

8.1. Unstrengthened arch (US)

The experimental tests for the case of the unstrengthened arch reported in [51] lead to the observation that the collapse is due to the opening of four flexural hinges according to the sequence reported in Table 8.

The opening sequence and positions of the hinges identified in the numerical simulations coincide with those experimentally observed (except for a slight difference of the position of the last hinge) and with the numerical results reported in [50]. On the other hand, a significant discrepancy of the present results, with respect to previous numerical simulations reported in [39], is encountered. Precisely, the proposed model seems to be more adherent to the experimental evidence with respect to the model proposed in [39]. In Figure 20 the capacity curves obtained with the present approach and the model proposed in [39] are compared with the envelope of the load displacement curves obtained with the two experiments [50], also showing the correspondence with the opening sequence of the four hinges, till the collapse condition reported in Figure 21.

Table 8. Hinge opening sequence for the US arch tests

Hinge	*Experimental tests [50]*		*Basilio [50]*		*Bertolesi et al.[39]*		*Proposed model*	
	Typology	*Position [mm]*	*Typology*	*Position [mm]*	*Typology*	*Position [mm]*	*Typology*	*Position [mm]*
H1	Flexural – intrados	355	Flexural – intrados	397	Flexural – intrados	397	Flexural – intrados	397
H2	Flexural – intrados	1517	Flexural – intrados	1517	Flexural – extrados	30	Flexural – intrados	1517
H3	Flexural – extrados	1087	Flexural – extrados	1120	Flexural – intrados	1517	Flexural – extrados	1120
H4	Flexural - extrados	57	Flexural - extrados	57	Flexural - extrados	1120	Flexural - extrados	30

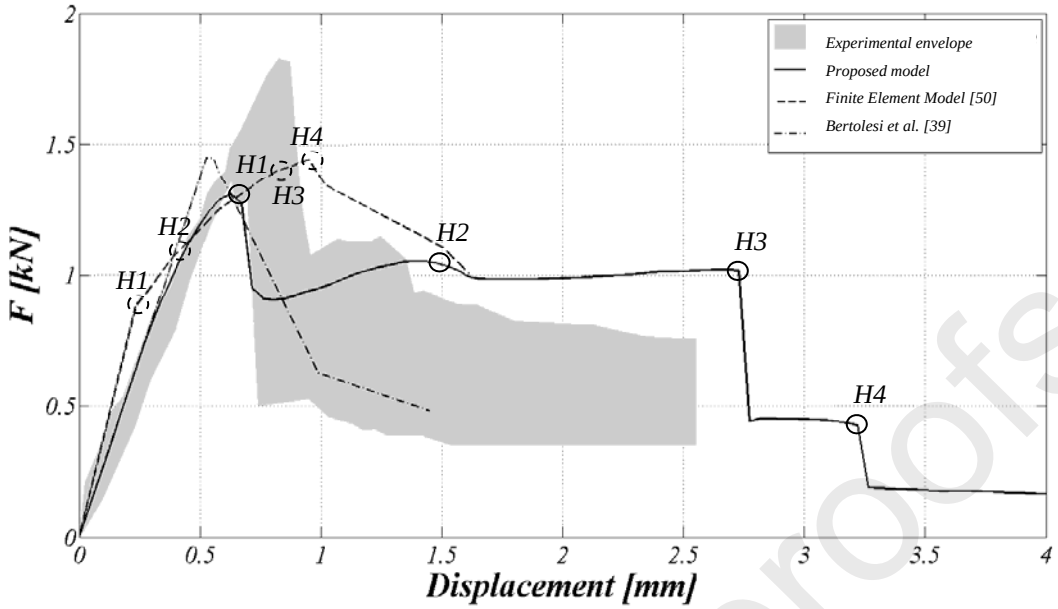

Figure 20. Comparison of the capacity curves for the US arch.

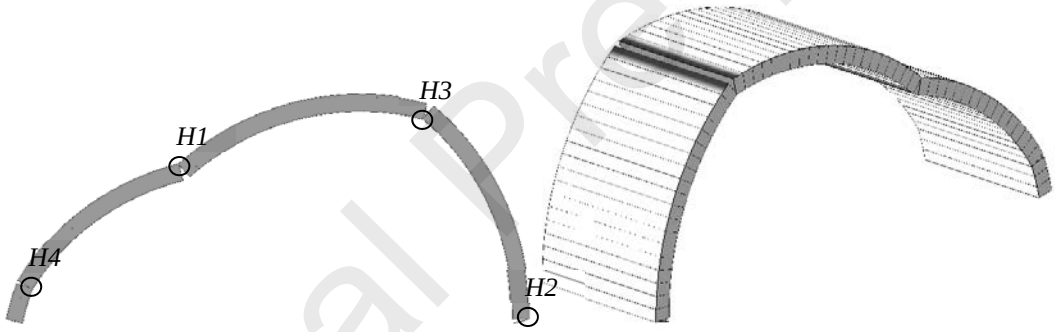

Figure 21. Collapse mechanism of the US arch.

8.2. Locally strengthened arch (LS)

The experimental tests for the case of the locally strengthened arch [50] lead to the observation that the collapse is due to the opening of four flexural hinges according to the opening sequence reported in Table 9. With respect to the unstrengthened arch, in this case

the presence of the FRP reinforcement implies a shift of the flexural hinges and leads to a higher carrying capacity.

In Figure 22 and Figure 23 the obtained results show a good agreement with the experimental tests in terms of capacity curve, collapse mechanism, damage pattern and evolution.

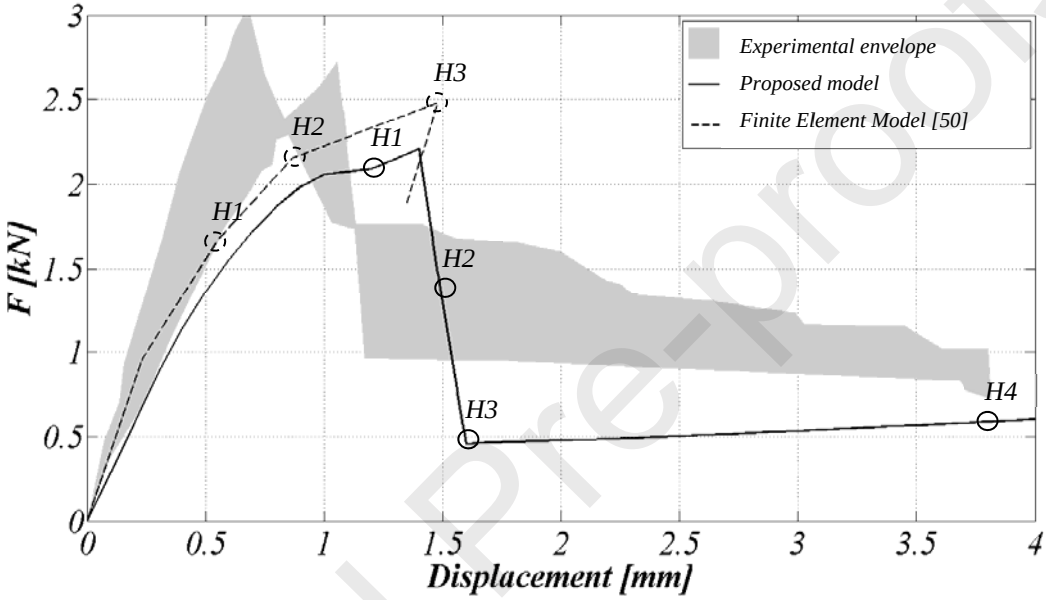

Figure 22. Comparison of the pushover curves for the LS arch.

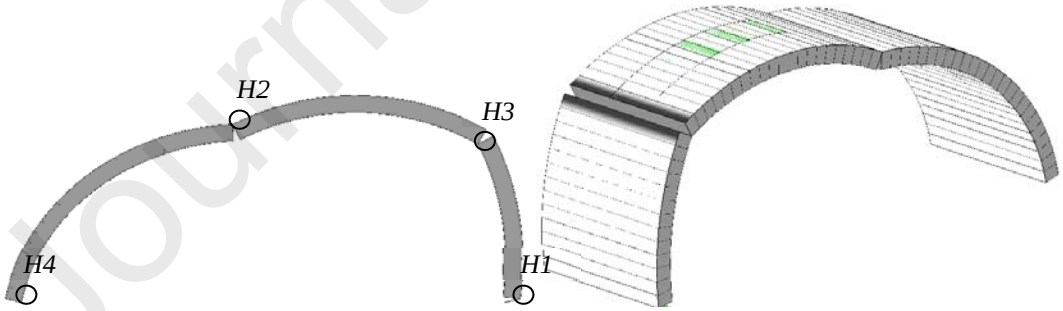

Figure 23. Collapse mechanism of the LS arch.

Table 9. Hinge opening sequence for the LS arch tests

Hinge	*Experimental tests [50]*		*Basilio [50]*		*Proposed model*	
	Typology	*Position [mm]*	*Typology*	*Position [mm]*	*Typology*	*Position [mm]*
H1	Flexural – intrados	1517	Flexural – intrados	1517	Flexural – intrados	1517
H2	Flexural – intrados	775	Flexural – extrados	1293	Flexural – intrados	600
H3	Flexural – extrados	1341	Flexural - extrados	0	Flexural – extrados	1293
H4	Flexural - extrados	0	-	-	Flexural - extrados	0

8.3. Continuously strengthened arches at the extrados (CSEa and CSEb)

The experimental tests for the case of arch strengthened at the extrados lead to a more complex collapse mechanism involving both flexural and shear hinges. The collapse configuration and the hinge opening sequence is described in detail in Table 10. In this case the different FRP reinforcement layouts do not modify the collapse mechanism, but simply increase the global strength and ductility. The results obtained in terms of hinge opening sequence with the proposed model show a good agreement with those of the experimental campaign; a slight shift of the hinge locations is encountered only.

In Figure 24 the proposed model shows a good match with the experimentally observed peak load in both the reinforcement configurations; on the other hand, the experimental results show a higher ductility which is not reproduced by any of the other reported numerical simulations, characterised by a comparable accuracy of the present approach.

It is also worth mentioning that in the case of the bond-slip tests, which are conducted on smaller specimens and therefore more manageable and verifiable, the proposed approach, whose simulations were reported in section 6, exhibits a satisfactory reliability.

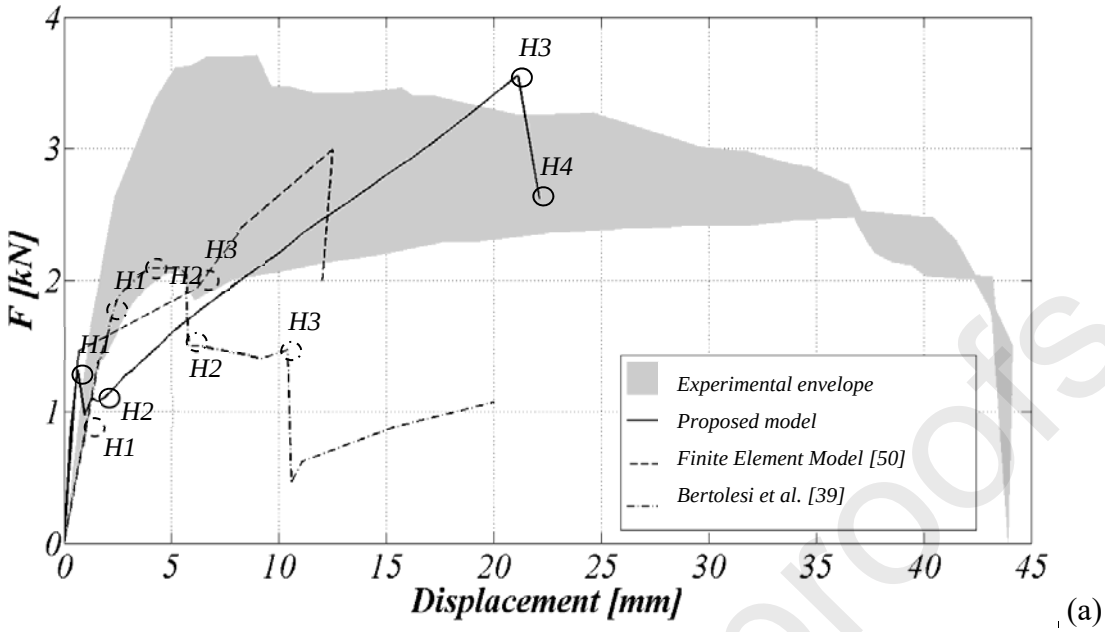

(a)

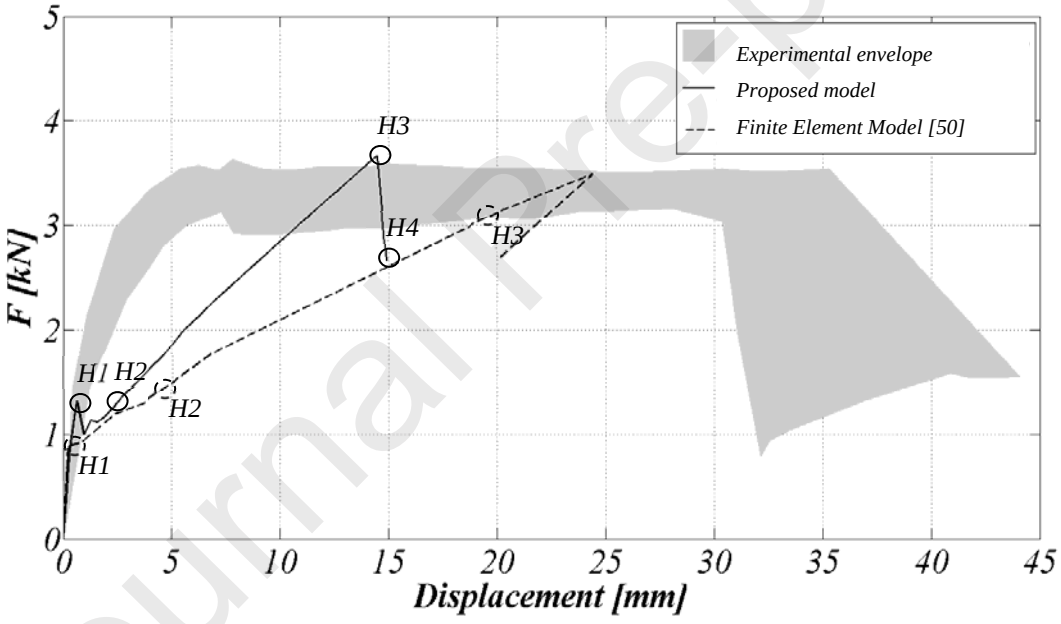

(b)

Figure 24. Comparison of the capacity curves for the arches reinforced at the extrados: (a) CSEa and (b) CSEb.

Table 10. Hinges opening sequence for the CSEa and CSEb arches

Hinge	*Experimental tests [50]*		*Basilio [50]*		*Bertolesi et al.(only CSEa) [39]*		*Proposed model*	
	Typology	*Position [mm]*	*Typology*	*Position [mm]*	*Typology*	*Position [mm]*	*Typology*	*Position [mm]*
H1	Flexural – intrados	330	Flexural – intrados	366	Flexural – intrados	366	Flexural – intrados	366
H2	Flexural – intrados	1517	Flexural – intrados	1517	Flexural – extrados	43	Flexural – intrados	1517
H3	Shear	330	Flexural - extrados	43	Flexural – intrados	1508	Shear	366
H4	Flexural - extrados	0	-	-	Flexural - extrados	1120	Flexural - extrados	43

In Figure 25 the red lines correspond to a shear hinge, occurred with the yielding along the tangential direction at one of the interfaces, which was also experimentally observed.

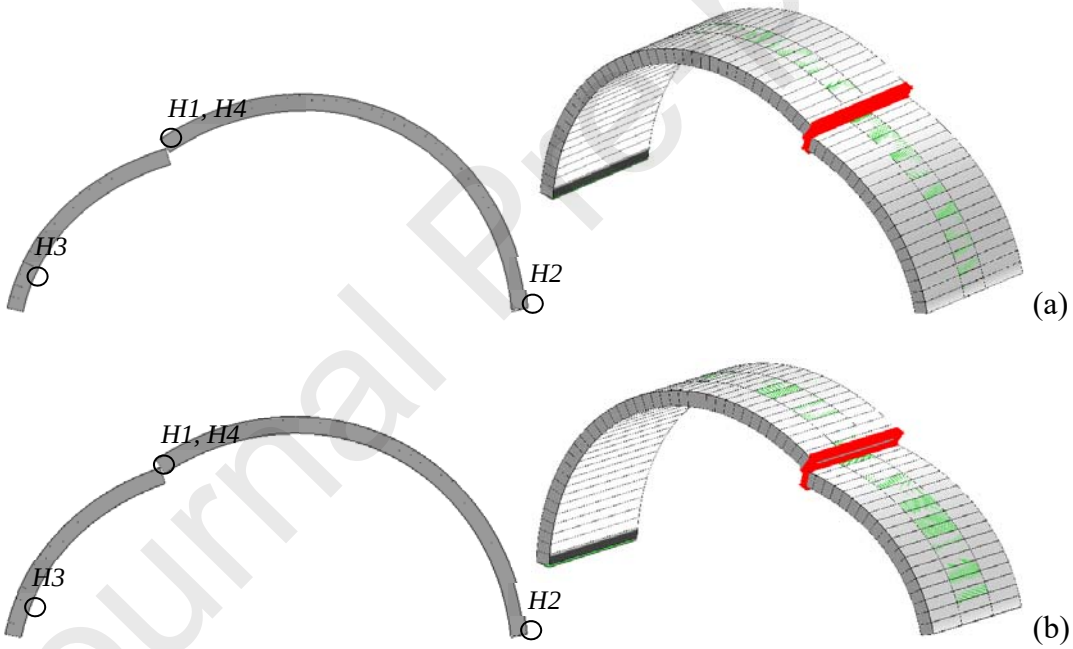

Figure 25. Collapse mechanism of the (a) CSEa and (b) CSEb arches.

8.4. Continuously strengthened arch at the intrados (CSI)

The experimental tests for the case of the arch continuously strengthened at the intrados lead to the observation that the collapse is due to the opening of four flexural hinges according to the opening sequence reported in **Error! Reference source not found.**. However, in this case the carrying capacity is mainly governed by the delamination phenomenon at the interface between the FRP reinforcement and the masonry. In this case the opening hinge sequence obtained with the proposed model is quite different from those obtained by the experimental results and by the numerical simulations in [50].

In Figure 26 the capacity curves obtained with the numerical simulations, in spite of the discrepancy in terms of opening sequence of the plastic hinges, matches the experimental envelope in terms of initial stiffness, peak load and displacement capacity.

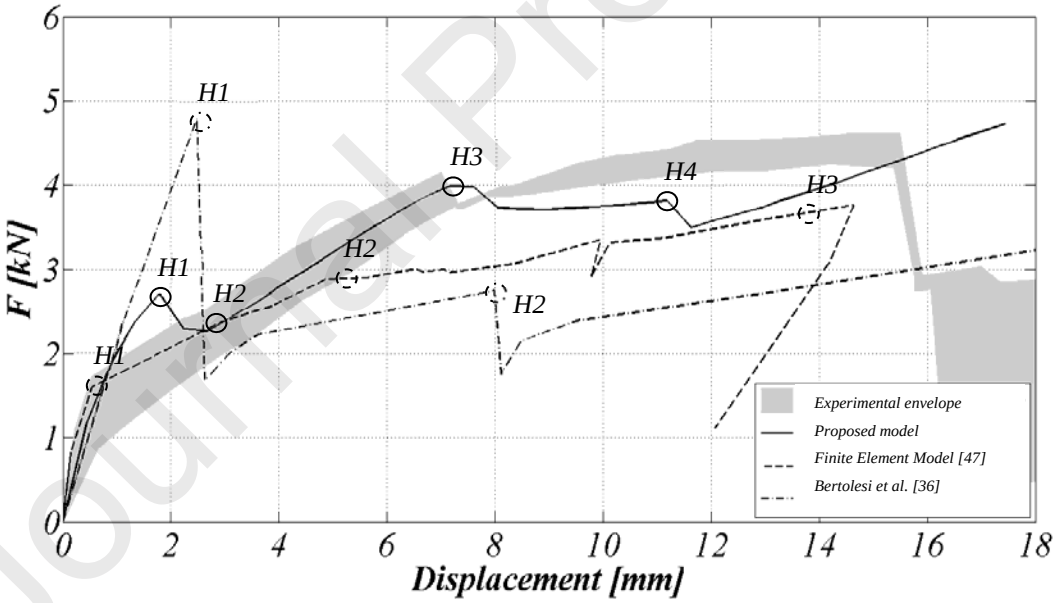

Figure 26. Comparison of the pushover curves for the CSI arch.

In Figure 27 the red lines correspond to the occurrence of delamination between the fibre reinforced strips and the masonry support. The ultimate load of the reinforced arch attained by the capacity curve in Figure 27 can be attributed to the occurrence of the delamination phenomenon which starts to propagate as the third flexural hinge opens.

Table 11. Hinges opening sequence for the CSI arches

Hinge	*Experimental tests [50]*		*Basilio [50]*		*Bertolesi et al. [39]*		*Proposed model*	
	Typology	*Position [mm]*	*Typology*	*Position [mm]*	*Typology*	*Position [mm]*	*Typology*	*Position [mm]*
H1	Flexural – extrados	1167	Flexural – extrados	1120	Flexural – intrados	366	Flexural – extrados	1120
H2	Flexural – intrados	1517	Flexural – intrados	1517	Flexural – extrados	43	Flexural – extrados	43
H3	Flexural – extrados	0	Flexural – extrados	43	Flexural – extrados	1508	Flexural – intrados	366
H4	-	-	-	-	Flexural - extrados	1120	Flexural - intrados	1508

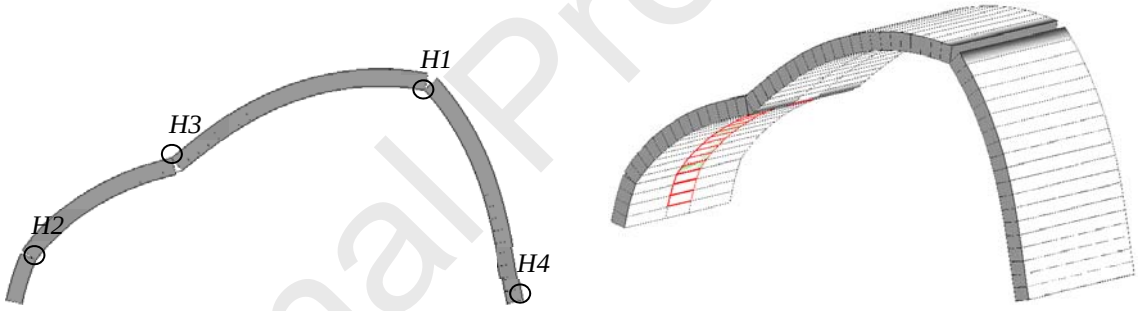

Figure 27. Collapse mechanism of the CSI arch.

9. Conclusions

In this paper a numerical strategy to assess the structural behaviour of masonry structures retrofitted by means of the application of EBC strips is presented. The proposed approach can be considered within the larger framework of the discrete macro-element strategies.

In particular, masonry is modelled by means of a discrete macro-element already proposed by the same authors in previous works. On the other hand, the EBC strips are modelled by means of a novel specific flat discrete element which can interact with other EBC elements (along the edges) and with masonry elements (through the contact surface) by means of continuous interfaces whose calibration procedures are extensively presented. Although simplified, the proposed strategy possesses the following features:

i) it is able to distinguish the correct damage propagation in the EBC-masonry interface (proper of mode II failure);

ii) it is able to grasp the effect of its actual geometric disposal: layers (strips) on the front (rear) of the masonry element, parallel (not parallel) to the masonry element edges, on the perimeter along the thickness of the masonry element, and also the case of overlapping textiles;

iii) it allows a three-dimensional disposal of the reinforcements;

iv) it requires a limited computational effort with respect to classic FEM approaches, because of the conceived parsimonious strategy;

v) the limit of the presented model is strictly related to the adoption of simple partially uncoupled uni-axial constitutive laws; however, the formulation of the proposed interfaces has been devised to accommodate alternative constitutive behaviours according to the desired detail and to the problem at hand;

vi) the adoption of uni-axial constitutive laws strongly increases the robustness of the numerical approach;

vii) although based on constitutive uni-axial constitutive laws the three-dimensional behaviour of the structural model is assured.

The suitability and reliability of the proposed approach was tested both on local models and whole structural elements (out-of-plane loaded panels and arches). Several comparisons are presented considering experimental tests and numerical results which employ both simplified and more detailed approaches. In all the considered cases the proposed model is able to describe accurately the non-linear behaviour of the EBC-reinforced masonry systems experimentally observed, and the results are comparable with those obtained with the advanced numerical simulations which make use of refined FE approaches.

Acknowledgements

This research was partially funded by the University of Catania, with the following projects: - "Linea di intervento 2 e Starting Grant del Piano di incentivi per la ricerca di Ateneo 2020/2022" of the Departments of Civil Engineering and Architecture (project “FIBER-HMS: FRCM-masonry Interaction: a novel approach for modelling the BEhaviour of Retrofitted Historical Masonry Structures”). - Progetto DPC-ReLUIS 2022-2024 WP5: Interventi di rapida esecuzione a basso impatto ed integrati.

References

[1] Di Tommaso A, Focacci F, Micelli F. Strengthening historical masonry with FRP or FRCM: Trends in design approach. Key Eng Mat 2017;747:166-73.

[2] Papanicolaou CG, Triantafillou TC, Karlos K, Papathanasiou M. Textile-reinforced mortar (TRM) versus FRP as strengthening material of URM walls: in-plane cyclic loading. Mater Struct 2007;40:1081–97.

[3] Papanicolaou CG, Triantafillou TC, Papathanasiou M, Karlos K. Textile reinforced mortar (TRM) versus FRP as strengthening material of URM walls: out-of-plane cyclic loading. Mater Struct 2008;41:143–57.

[4] Capozucca R. Experimental FRP/SRP-historic masonry delamination. Compos Struct 2010;92(4):891-903.

[5] Fedele R, Milani G. Three-dimensional effects induced by FRP-from-masonry delamination. Compos Struct 2011;93(7):1819-31.

[6] Carloni C, Subramaniam KV. FRP-masonry debonding: Numerical and experimental study of the role of mortar joints. J Compos Constr 2012;16(5):581-89.

[7] Valluzzi MR, Oliveira DV, Caratelli A, Castori G, Corradi M, De Felice G, Garbin E, Garcia D, Garmendia L, Grande E, Ianniruberto U, Kwiecień A, Leone M, Lignola GP, Lourenço PB, Malena M, Micelli F, Panizza M, Papanicolaou CG, Prota A, Sacco E, Triantafillou TC, Viskovic A, Zając B, Zuccarino G. Round Robin Test for composite-to-brick shear bond characterization. Mater Struct 2012;45(12):1761-91.

[8] Napoli A, de Felice G, De Santis S, Realfonzo R. Bond behaviour of Steel Reinforced Polymer strengthening systems. Compos Struct 2016;152:499-515.

[9] Marcari G, Manfredi G, Prota A, Pecce M. In-plane shear performance of masonry panels strengthened with FRP. Compos Part B-Eng 2007;38(7-8):887-901.

[10] Bui T-L, Si Larbi A, Reboul N, Ferrier E. Shear behaviour of masonry walls strengthened by external bonded FRP and TRC. Compos Struct 2015;132:923-32.

[11] Gilstrap JM, Dolan CW. Out of plane bending of FRP-reinforced masonry walls. Compos Sci Technol 1998;58(8):1277-84.

[12] Griffith MC, Kashyap J, Mohamed Ali MS, Flexural displacement response of NSM FRP retrofitted masonry walls. Constr Build Mater 2013;49:1032-40.

[13] Oliveira DV, Basilio I, Lourenço PB. Experimental behavior of FRP strengthened masonry arches. J Compos Constr 2010;14(3):312-22.

[14] Valluzzi MR, Valdemarca M, Modena C. Behavior of brick masonry vaults strengthened by FRP laminates. J Compos Constr 2001;5(3):163-69.

[15] Alcaino P, Santa-Maria H, Experimental response of externally retrofitted masonry walls subjected to shear loading. J Compos Constr 2008;12(5):489-98.

[16] Lignola GP, Prota A, Manfredi G. Numerical investigation on the influence of frp retrofit layout and geometry on the in-plane behavior of masonry walls. J Compos Constr 2012;16(6):712-23.

[17] Stratford T, Pascale G, Manfroni O, Bonfiglioli B. Shear strengthening masonry panels with sheet glass-fiber reinforced polymer. J Compos Constr 2004;8(5):434-43.

[18] Oliveira DV, Basilio I, Lourenço PB. Experimental bond behavior of FRP sheets glued on brick masonry J Compos Constr 2011;15(1):32-41.

[19] Ascione L, De Felice G, De Santis S. A qualification method for externally bonded Fibre Reinforced Cementitious Matrix (FRCM) strengthening systems. Compos Part B-Eng 2015;78:497-506.

[20] CNR-DT 215/2018. Istruzioni per la Progettazione, l'Esecuzione ed il Controllo di Interventi di Consolidamento Statico mediante l'utilizzo di Compositi Fibrorinforzati a Matrice Inorganica. C.N.R., National Research Council, Italy; 2006.

[21] CNR-DT 200 R1/2013. Guide for the Design and Construction of Externally Bonded FRP Systems for Strengthening Existing Structures. C.N.R., National Research Council, Italy; 2013.

[22] Yuan H, Lu X, Hui D, Feo L. Studies on FRP-concrete interface with hardening and softening bond-slip law. Compos Struct 2012;94 (12):3781-92.

[23] Ferracuti B, Savoia M, Mazzotti C, Interface law for FRP-concrete delamination. Compos Struct 2007;80(4):523-31.

[24] de Felice G, Aiello MA, Bellini A, Ceroni F, De Santis S, Garbin E, Leone M, Lignola GP, Malena M, Mazzotti C, Panizza M, Valluzzi MR. Experimental characterization of composite-to-brick masonry shear bond. Mater Struct 2016;49(7):2581-96.

[25] Ceroni F, de Felice G, Grande E, Malena M, Mazzotti C, Murgo F, Sacco E, Valluzzi MR. Analytical and numerical modeling of composite-to-brick bond. Mater Struct 2014;47(12):1987-2003.

[26] Bertolli V, D'Antino T. Modeling the behavior of externally bonded reinforcement using a rigid-trilinear cohesive material law. Int J Solids Struct 2022;248:111641.

[27] Malena M, Focacci F, Carloni C, de Felice G. The effect of the shape of the cohesive material law on the stress transfer at the FRP-masonry interface. Compos Part B-Eng 2017;110:368-80.

[28] Malena M, de Felice G. Debonding of composites on a curved masonry substrate: Experimental results and analytical formulation. Compos Struct 2014;112(1):194-206.

[29] Grande E, Milani G. Interface modeling approach for the study of the bond behaviour of FRCM strengthening systems. Compos Part B-Eng 2018;141:221-23.

[30] Bertolesi E, Grande E, Milani G. Numerical modeling of the bond behaviour of FRCM systems externally applied to masonry substrates. J Build Rehabil 2019;4(4).

[31] Mazzucco G, D'Antino T, Pellegrino C, Salomoni V. Three-dimensional finite element modeling of inorganic-matrix composite materials using a mesoscale approach. Compos Part B-Eng 2018;143:75-85.

[32] Ghiassi B, Oliveira DV, Lourenço PB, Marcari, G. Numerical study of the role of mortar joints in the bond behavior of FRP-strengthened masonry. Compos Part B-Eng 2013;46:21-30.

[33] Grande E, Milani G, Sacco E. Modelling and analysis of FRP-strengthened masonry panels. Eng Struct 2008;30(7):1842-60.

[34] Basilio I, Fedele R, Lourenço PB, Milani G. Numerical and experimental analysis of full scale arches reinforced with GFRP materials. Key Eng Mat 2015;624:502-09.

[35] Maruccio C, Basilio I, Oliveira DV, Lourenço, PB, Monti G. Numerical modelling and parametric analysis of bond strength of masonry members retrofitted with FRP. Constr Build Mater 2014;73:713-27.

[36] Milani G, Milani E, Tralli A. Upper bound limit analysis model for FRP-reinforced masonry curved structures. Part II: Structural analyses. Comput Struct 2009;87(23-24):1534-58.

[37] Caporale A, Feo L, Hui D, Luciano R. Debonding of FRP in multi-span masonry arch structures via limit analysis. Compos Struct 2014;108(1):856-65.

[38] Bati SB, Fagone M, Rotunno T. Lower bound limit analysis of masonry arches with CFRP reinforcements: A numerical method. J Compos Constr 2013;17(4):543-53.

[39] Bertolesi E, Milani G, Fedele R. Fast and reliable FE approach for the analysis of FRP-reinforced masonry arches. Compos Part B-Eng 2016;88:189-200.

[40] Milani G, Lourenço PB. Simple Homogenized Model for the Non-linear Analysis of FRP-Strengthened Masonry Structures. I: Theory. J Eng Mech 2013;139(1):59-76.

[41] Milani G, Lourenço PB. Simple Homogenized Model for the Non-linear Analysis of FRP-Strengthened Masonry Structures. II: Structural Applications. J Eng Mech 2013;139(10):77-93.

[42] Scacco J, Ghiassi B, Milani G, Lourenço PB. A fast modeling approach for numerical analysis of unreinforced and FRCM reinforced masonry walls under out-of-plane loading. Compos Part B-Eng 2020;180:107553.

[43] Caddemi S, Caliò I, Cannizzaro F, Pantò B. New frontiers on seismic modeling of masonry structures. Frontiers in Built Environment 2017;3:39.

[44] Cannizzaro F, Pantò B, Caddemi S, Caliò I, A Discrete Macro-Element Method (DMEM) for the non-linear structural assessment of masonry arches. Eng Struct 2018;168:243-56.

[45] Caliò I, Cannizzaro F, Marletta M. A discrete element for modeling masonry vaults. Adv Mat Res 2010;133-134:447-52.

[46] Caliò I, Marletta M, Pantò B. A new discrete element model for the evaluation of the seismic behaviour of unreinforced masonry buildings. Eng Struct 2012;40:327-338.

[47] Caddemi S, Caliò I, Cannizzaro F, Lourenço PB, Pantò B. FRP-reinforced masonry structures: Numerical modeling by means of a new discrete element approach. COMPDYN 2017 - Proceedings of the 6th International Conference on Computational Methods in Structural Dynamics and Earthquake Engineering, 2017;1:2639-50.

[48] Pantò B, Cannizzaro F, Caddemi S, Caliò I, Chácara C, Lourenço PB. Non-linear modelling of curved masonry structures after seismic retrofit through FRP reinforcing. Buildings 2017;7(3):79.

[49] Padalu PKVR, Singh Y, Das S. Efficacy of basalt fibre reinforced cement mortar composite for out-of-plane strengthening of unreinforced masonry. Constr Build Mater 2018;191:1172-90.

[50] Basilio I. Strenghtening of arched masonry structures with composite materials. University of Minho, PhD Thesis in Civil Engineering 2007.

[51] Oliveira DV, Basilio I, Lourenço PB. Experimental behavior of FRP strengthened masonry arches. J Compos Constr 2010;14(3):312-22.

[52] Pantò B, Cannizzaro F, Caddemi S, Caliò I. 3D macro-element modelling approach for seismic assessment of historical masonry churches. Adv Eng Soft 2016;97:40-59.

[53] Pantò B, Cannizzaro F, Lourenço PB, Caliò I. Numerical and experimental validation of a 3D macro-model for the in-plane and out-of-plane behavior of unreinforced masonry walls. Int J Archit Herit 2017;11(7):946–64.

[54] Caddemi S, Caliò I, Cannizzaro F, Pantò B. A new computational strategy for the seismic assessment of infilled frame structures. Proceedings of the 2013 Civil-Comp Proceedings, Sardinia, Italy (2013): 3-6.

[55] Panto B, Silva L, Vasconcelos G, Lourenço PB. Macro-modelling approach for assessment of out-of-plane behavior of brick masonry infill walls. Eng Struct 2019;181:529-549.

[56] Caddemi S, Caliò I, Cannizzaro F, Pantò B. The seismic assessment of historical masonry structures. in B.H.V. Topping, P. Iványi, (Editors), Proceedings of the Twelfth International Conference on Civil, Structural and Environmental Engineering Computing, Civil-Comp Press, Stirlingshire, UK, 2014;77.

[57] HiStrA (Historical Structure Analysis). HISTRA s.r.l, Catania, Italy. Release 17.2.3, April 2015. http://www.histra.it.

[58] Turnsek V, Cacovic F. Some experimental result on the strength of brick masonry walls. in 2nd International Brick Masonry Conference. UK, Stoke-on-Trent, 1971.

[59] Cundall PA, Strack ODL. A discrete numerical model for granular assemblies. Geotechnique 1979;29(1):47-65.

[60] Casolo S, Peña F. Rigid element model for in-plane dynamics of masonry walls considering hysteretic behaviour and damage. Earthq Eng Struct D 2007;36(8):1029-48.

[61] Bertolesi E, Carozzi FG, Milani G, Poggi C. Numerical modeling of Fabric Reinforce Cementitious Matrix composites (FRCM) in tension. Constr Build Mater 2014;70:531-48.

[62] Bernardi P, Ferretti D, Leurini F, Michelini E. A non-linear constitutive relation for the analysis of FRCM elements. Procedia Structural Integrity 2 2016; 2674-81. 21st European Conference on Fracture, ECF21, 20-24 June 2016, Catania, Italy

[63] Monaco A, Minafò G, D'Anna J, Oddo MC, La Mendola L. Constitutive numerical model of FRCM strips under traction. Frontiers in Built Environment 2020;6(60).

[64] Cannizzaro F, Lourenço PB. Simulation of Shake Table Tests on Out-of-Plane Masonry Buildings. Part (VI): Discrete Element Approach. Int J Archit Herit 2017;11(1):125-42.

[65] Spacone E, Filippou FC, Taucer FF. Fibre beam-column model for non-linear analysis of R/C frames: Part I. Formulation. Earthq Eng Struct D 1996;25(7):711-25.

[66] Caballero A, Willam KJ, Carol I. Consistent tangent formulation for 3D interface modelling of cracking/fracture in quasi-brittle materials. Comput Method Appl M 2008; 197:2804–22.

[67] Macorini L, Izzuddin BA. A non-linear interface element for 3D mesoscale analysis of brick-masonry structures. Int J Numer Meth Eng 2011;85:1584-1608.

[68] Minga E, Macorini L, Izzuddin BA. A 3D mesoscale damage-plasticity approach for masonry structures under cyclic loading. Meccanica 2018;53:1591–1611.

[69] Mazzucco G, D'Antino T, Salomoni V, Carloni C. A Cohesive Contact Algorithm to Describe the Multi-axial Bond Behavior of FRCM Composites. In: Ilki, A., Ispir, M., Inci, P. (eds) 10th International Conference on FRP Composites in Civil Engineering. CICE 2021. Lecture Notes in Civil Engineering, vol 198. Springer, Cham.

[70] Marini A, Spacone E. Analysis of reinforced concrete elements including shear effects. ACI Struct J 2006;103(5):645–655.

[71] Cannizzaro F, Pantò B, Caddemi S, Caliò I, Macorini L, Izzuddin B. Alternative strategies for modelling masonry arches. Fourteenth International Conference on Computational Structures Technology Civil Comp 2022, Montpellier (France) August 23- 25 2022.

[72] Lourenço PB, Rots JG. A multi-surface interface model for the analysis of masonry structures. J Eng Mech 1997;123(7):660–68.

[73] Padalu PKVR, Singh Y, Das S. Out-of-plane flexural behaviour of masonry wallettes strengthened using FRP composites and externally bonded grids: Comparative study. Compos Part B-Eng 2019;176:107302.

[74] Jahangir H, Esfahani MR. Numerical Study of Bond – Slip Mechanism in Advanced Externally Bonded Strengthening Composites. KSCE J Civ Eng 2018:22(11):4509-18.

APPENDIX A: Reference systems and matrix operators of the EBC-EBC interface

The degrees of freedom of the generic *r*-th EBC element collected in the vector $\mathbf{d}_r^T = \begin{bmatrix} U_r & V_r & W_r & \Phi_r & \Theta_r & \Psi_r \end{bmatrix}$ are referred to a local reference system ($\mathbf{e}_{rx}, \mathbf{e}_{ry}, \mathbf{e}_{rz}$), centred at the centre of gravity G, being $\mathbf{e}_{rx}$ and $\mathbf{e}_{ry}$ orthogonal unit vectors lying on the plane of the EBC element and $\mathbf{e}_{rz}$ the orthogonal direction. In particular, $\mathbf{e}_{rx}$ is parallel to the direction of the fibres embedded in the EBC element.

The 12 auxiliary local degrees of freedom of the EBC-EBC interface connecting the *r*-th and *s*-th EBC elements, $\bar{\mathbf{u}}_r^T = \begin{bmatrix} u_r & v_r & w_r & \phi_r & \theta_r & \psi_r \end{bmatrix}$ and $\bar{\mathbf{u}}_s^T = \begin{bmatrix} u_s & v_s & w_s & \phi_s & \theta_s & \psi_s \end{bmatrix}$, are referred to a local reference system ($\mathbf{e}_\xi, \mathbf{e}_\eta, \mathbf{e}_\zeta$) with origin at the midpoint Ω of the EBC-EBC interface described as follows: the unit vector $\mathbf{e}_\xi$ indicates the axis oriented along the line interface direction, the unit vector $\mathbf{e}_\zeta$ represents the average direction between the two unit vectors orthogonal to the edges of two connected *r* and *s* EBC elements, whereas $\mathbf{e}_\eta$ is obtained by the cross product between $\mathbf{e}_\zeta$ and $\mathbf{e}_\xi$.

The 6×6 compatibility matrix operators $\mathbf{A}_r, \mathbf{A}_s$ introduced in Eq. (3) to express $\bar{\mathbf{u}}_r, \bar{\mathbf{u}}_s$ in terms of $\mathbf{d}_r, \mathbf{d}_s$, respectively, are be defined for the generic *r*-th EBC plate element as follows:

$$\mathbf{A}_r = \left[\begin{array}{c|c} \mathbf{R}_r & \mathbf{R}_r \cdot \mathbf{W}_r \\ \hline \mathbf{0}_{3,3} & \mathbf{R}_r \end{array}\right] \tag{A1}$$

where $\mathbf{R}_r$ is the transformation matrix able to relate the reference systems of the connected element and the interface, while $\mathbf{W}_r$ is the skew matrix of the vector identifying the position of the origin of the reference system of the interface. Such matrices are defined as follows:

$$\mathbf{R}_r = \begin{bmatrix} \mathbf{e}_{rx}\cdot\mathbf{e}_{\xi} & \mathbf{e}_{ry}\cdot\mathbf{e}_{\xi} & \mathbf{e}_{rz}\cdot\mathbf{e}_{\xi} \\ \mathbf{e}_{rx}\cdot\mathbf{e}_{\eta} & \mathbf{e}_{ry}\cdot\mathbf{e}_{\eta} & \mathbf{e}_{rz}\cdot\mathbf{e}_{\eta} \\ \mathbf{e}_{rx}\cdot\mathbf{e}_{\varsigma} & \mathbf{e}_{ry}\cdot\mathbf{e}_{\varsigma} & \mathbf{e}_{rz}\cdot\mathbf{e}_{\varsigma} \end{bmatrix}; \qquad \mathbf{W}_r = \begin{bmatrix} 0 & z_{\Omega} - z_{G_r} & y_{G_r} - y_{\Omega} \\ z_{G_r} - z_{\Omega} & 0 & x_{\Omega} - x_{G_r} \\ y_{\Omega} - y_{G_r} & x_{G_r} - x_{\Omega} & 0 \end{bmatrix} \tag{A2}$$

$\mathbf{R}_s$ and $\mathbf{W}_s$ are defined analogously.

APPENDIX B: Matrix operators of the EBC-EBC interface

The compatibility matrices A_r, A_p appearing in Eq. (8), to link the auxiliary degrees of freedom of the interface with those of the connected elements, are dependent on the geometry of the elements as follows:

$$\mathbf{A}_r = \left[\mathbf{I}_6\right] \tag{B1}$$

$$\mathbf{A}_p = \left[\begin{array}{c|c|c} \mathbf{R} & \mathbf{R}\cdot\mathbf{W} & \mathbf{R}\cdot\mathbf{d}_\Gamma \\ \hline \mathbf{0}_{3,3} & \mathbf{R} & \mathbf{0}_{3,1} \end{array}\right] \tag{B2}$$

where $\mathbf{I}_6$ is the identity matrix of order 6 and $\mathbf{R}$ and $\mathbf{W}$, analogously to what already introduced in Eq. (A2), are defined as follows:

$$\mathbf{R} = \begin{bmatrix} \mathbf{e}_{px}\cdot\mathbf{e}_{rx} & \mathbf{e}_{py}\cdot\mathbf{e}_{rx} & \mathbf{e}_{pz}\cdot\mathbf{e}_{rx} \\ \mathbf{e}_{px}\cdot\mathbf{e}_{ry} & \mathbf{e}_{py}\cdot\mathbf{e}_{ry} & \mathbf{e}_{pz}\cdot\mathbf{e}_{ry} \\ \mathbf{e}_{px}\cdot\mathbf{e}_{rz} & \mathbf{e}_{py}\cdot\mathbf{e}_{rz} & \mathbf{e}_{pz}\cdot\mathbf{e}_{rz} \end{bmatrix}; \qquad \mathbf{W} = \begin{bmatrix} 0 & z_{G_r} - z_{G_p} & y_{G_p} - y_{G_r} \\ z_{G_p} - z_{G_r} & 0 & x_{G_r} - x_{G_p} \\ y_{G_r} - y_{G_p} & x_{G_p} - x_{G_r} & 0 \end{bmatrix} \tag{B3}$$

being the coordinates of G_p and G_r expressed in the local reference system of the masonry panel. The vector $\mathbf{d}_\Gamma$ appearing in Eq. (B2) collects the displacements components of G_r in the local reference systems of the masonry element associated with a unit distortion of the degree of freedom Γ_p, and can be defined as follows:

$$\mathbf{d}_{\Gamma}\left(u_{G_r},v_{G_r}\right)=\begin{bmatrix}\dfrac{\left(1+u_{G_r}\right)\left(1+v_{G_r}\right)}{4}\left(-l_4\dfrac{\sin\alpha_4}{\sin\alpha_3}\sin\alpha_2\right)+\dfrac{\left(1-u_{G_r}\right)\left(1+v_{G_r}\right)}{4}\left(-l_4\sin\alpha_1\right)\\ \dfrac{\left(1+u_{G_r}\right)\left(1+v_{G_r}\right)}{4}\left(-l_4\dfrac{\sin\alpha_4}{\sin\alpha_3}\cos\alpha_2\right)+\dfrac{\left(1-u_{G_r}\right)\left(1+v_{G_r}\right)}{4}\left(l_4\cos\alpha_1\right)\\ 0\end{bmatrix} \tag{B4}$$

In Eq.(B4) $\left(u_{G_r},v_{G_r}\right)$ are the coordinates of the projection of G_r on the average plane of the panel in an intrinsic local reference system u,v $\left(u\in[-1,1],v\in[-1,1]\right)$. $l_i,i=1,...,4$ and $\alpha_i,i=1,...,4$ represent the length of the *i*-th edge and the angle at the *i*-th vertex of the masonry element, respectively.

Francesco Cannizzaro: Conceptualization, methodology, software, validation, data curation, Writing - Original Draft, visualization, funding acquisition.
Bartolomeo Pantò: Conceptualization, methodology, software, Writing - Review & Editing, visualization.
Salvatore Caddemi: Conceptualization, methodology, formal analysis, Writing - Original Draft, funding acquisition.
Ivo Caliò: Conceptualization, methodology, Writing - Review & Editing, supervision, funding acquisition.

June 28, 2021

Dear Editor,

On behalf of the authors of the manuscript entitled “Discrete modelling of fibre reinforced composites layers on masonry structures”, I declare that there are no conflict of interest for its publication in the Composite Structures.

Best regards,

Francesco Cannizzaro, PhD
Department of Civil Engineering and Architecture
University of Catania

Declaration of interests

☒ The authors declare that they have no known competing financial interests or personal relationships that could have appeared to influence the work reported in this paper.

☐The authors declare the following financial interests/personal relationships which may be considered as potential competing interests: